Remote Sensing of Environment 277 (2022) 113038

Contents lists available at ScienceDirect

Remote Sensing of Environment

journal homepage: www.elsevier.com/locate/rse

A new approach for 2-D and 3-D precise measurements of ground deformation from optimized registration and correlation of optical images and ICA-based filtering of image geometry artifacts

Saif Aati [a,b,*], Chris Milliner [a], Jean-Philippe Avouac [a]

[a] California Institute of Technology, CA, USA
[b] Univ. Gustave Eiffel - IGN/ENSG, LaSTIG Lab., France

ARTICLE INFO

Editor: Jing M. Chen

Keywords:
Sub-pixel image correlation
Rigorous sensor model
2D/3D surface displacement
ICA

ABSTRACT

High resolution satellite images with improved spatial and temporal resolution provide unprecedented opportunities to monitor Earth Surface changes in 2D and 3D due, for example, to earthquakes, sand dune migration, ice flow, or landslides. The volume of imagery available for such measurements is rapidly growing but the exploitation of these data is challenging due to the various sources of geometric distortions of the satellite imagery. Here we propose a new approach to extract high-quality surface displacement in 3D based on the correlation of multi-date and multi-platform high resolution optical imagery. We additionally show that when a large enough volume of data is available, it is possible to separate the deformation signal from the artifacts due to the satellite jitter and misalignment of the CCDs, which, together with topographic artifacts, are the main source of noise in the measurements. Our method makes use of a reference DEM, but the outcome is independent of the characteristics of the chosen DEM. We use the case-example of the ground deformation caused by the Ridgecrest earthquake sequence to assess the performance of our proposed approach. We show that it outperforms the more standard approach which combines 2-D correlation and DEM differencing. With our technique, we were able to generate high quality measurements of coseismic ground displacement with GSD of 2.4 m, and uncertainties at the 90% confidence level on the NS, EW and vertical displacement measurements of 0.6 m, 0.7 m, and 0.6 m respectively.

1. Introduction

Satellite optical images can be used to measure surface displacements in 2-D and 3-D due for example to earthquakes, sand dune migration, ice flow, or landslides, (e.g., Altena and Kääb, 2017; Antoine et al., 2021; Avouac and Leprince, 2015; Barišin et al., 2015; Bontemps et al., 2018; Stumpf et al., 2017, 2018; Zhou et al., 2015; Zinke et al., 2019). The volume of imagery available for such measurements is rapidly growing, and this has motivated various efforts of method development to complement the tools available for 2-D measurements such as COSI-Corr (Leprince et al., 2007) or MicMac (Rupnik et al., 2017). Optical images are generally taken with view angles less than 20° from nadir, so that they are more sensitive to horizontal than to vertical displacements. A common practice is to first calculate the 2-D displacements from correlating orthorectified images and determine vertical displacements next from differencing Digital Elevation Models (DEMs) produced with images acquired before and after the deformation event, (e.g., Antoine et al., 2021; Barnhart et al., 2020). Orthorectification errors are then a major source of noise in the measurements of the 2-D displacement field. One reason is that the DEMs used in the process generally don't have the adequate ground resolution to account for the stereoscopic disparities present in the raw images. In addition, topographic changes, due to vertical displacements or the advection of the topography associated with the horizontal displacements, can be a source of bias and errors on the measurements of horizontal displacements (Altena and Kääb, 2017; Ayoub et al., 2009), and vertical differencing represents vertical displacement only if the topography has no relief at the scale of the horizontal displacement or if the horizontal displacement is null. It should therefore be advantageous to correlate non-orthorectified images since it is in principle possible to separate stereoscopic disparities and ground displacements in 3-D. The principle is used widely in computer vision (e.g., Tang et al., 2019). For satellite

* Corresponding author at: California Institute of Technology, CA, USA.
E-mail address: saif@caltech.edu (S. Aati).

https://doi.org/10.1016/j.rse.2022.113038
Received 4 October 2021; Received in revised form 16 March 2022; Accepted 3 April 2022
Available online 30 April 2022

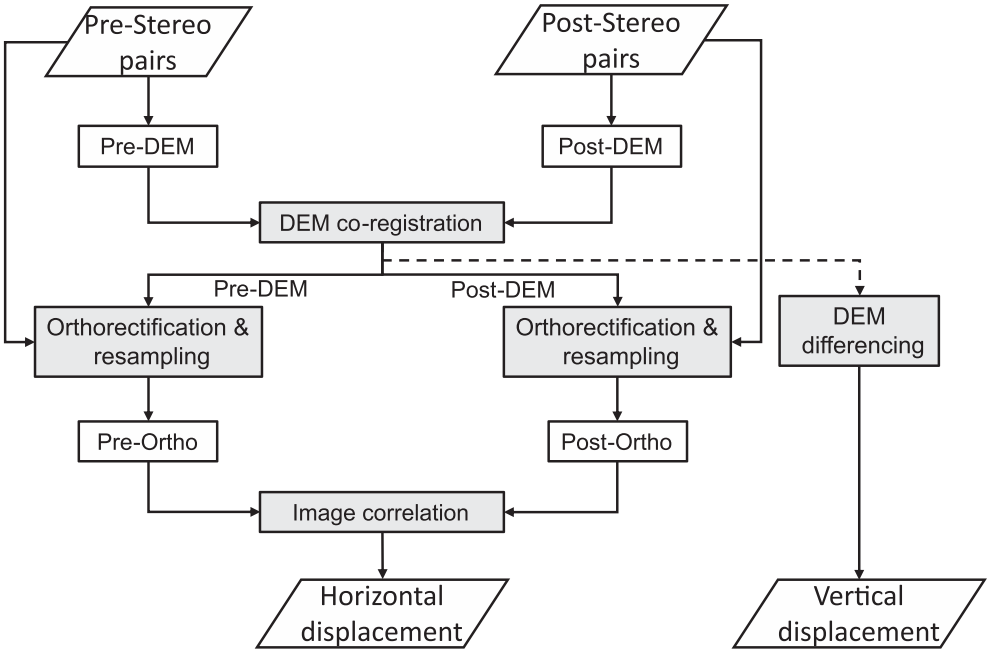

Fig. 1. State of the art method for 3-D displacement measurements using optical images.

images, a procedure was outlined by (Avouac and Leprince, 2015) (also applied, for example, by Zinke et al. (2019)) which requires stereoscopic pairs of images acquired before and after the deformation event.

Here we propose an alternative end-to-end approach to extract high-quality 2D/3D surface displacement. We additionally show that when a large enough volume of data is available, it is possible to separate the deformation signal from the artifacts due to the satellite jitter and misalignments of the Charge-Coupled Devices (CCDs), which, together with topographic artifacts, are the main source of noise in the measurement of ground deformation from satellite image correlation (Beyer et al., 2018; Leprince et al., 2007). Our procedure makes use of the Independent Component Analysis (e.g., Gualandi et al., 2016), which is an unsupervised Machine Learning algorithm. ICA is a blind source separation technique that allows extracting signals that would otherwise be camouflaged when the low-order statistical method of Principal Component Analysis (PCA) is adopted. It has been used for example to extract hydrological signals from gravimetric and geodetic data (e.g., Forootan et al., 2012; Larochelle et al., 2018), or, in remote sensing for hyperspectral image classification (Dalla Mura et al., 2011). In our study, we show a new application of ICA by demonstrating that geometric image artifacts can be filtered out with this technique. This is a crucial element of our workflow as it allows accurately measuring stereoscopic offsets for pair of images with low B/H, which is critical to improving the 2-D measurements and extracting the vertical displacement field. The ICA-based approach presented in this study thus provides an alternative or complementary approach to the state-of-the-art techniques that correct such artifacts during the orthorectification procedure (Leprince, 2008; Leprince et al., 2007; Shean et al., 2016). We show in this study that the proposed approach outperforms the state-of-the-art method, and allows the joint co-registration of images from different platforms and produces geometrically consistent data.

Hereafter, we first briefly describe how 2-D and 3-D displacements can be measured from the correlation of orthorectified images and DEM differencing, which is an approach that is commonly adopted. We next present our alternative approach and compare the two approaches based on an application to the large dataset covering the epicentral area of the M_w 7.1 Ridgecrest earthquake sequence, which occurred in California in July 2019.

2. State-of-the-art method for measuring ground displacements with optical images

Ground displacements in 2-D are generally measured from correlation of orthorectified images, ideally including some optimized registration and orthorectification procedures (e.g., Avouac and Leprince, 2015). The most common method for calculating 3D surface deformation is to independently solve for the horizontal and vertical displacements (Fig. 1). Ideally, to obtain a good quality deformation measurement, in-track stereo pairs before and after the event that caused the deformation (i.e., a landslide, earthquake, ice movement) are needed to generate distinct digital elevation models (DEMs): a pre-DEM that represents the topography prior to the event and a post-DEM that accounts for the topography changes after the event. In general, the DEMs produced at different epochs are not perfectly registered. Therefore, the two DEMs must be aligned and resampled on a common grid. In most instances, the alignment is achieved using a stable area away from the deformation (i.e., an area did not experience any topographic changes and the distribution of the difference ~ 0). Then, the pre-and post-raw images are orthorectified with the pre-and post-DEM, respectively. In practice, images with the smallest view angle are selected to minimize the stereoscopic effect on the derived ortho-image. The horizontal displacement is then derived from the image correlation technique, while the vertical displacement is derived by differencing the two aligned DEMs.

The Iterative Closet Point (ICP) approach method is generally used to align different sets of point clouds derived from airborne or terrestrial LiDAR data (Besl and McKay, 1992; Nissen et al., 2014) or photogrammetry (Shean et al., 2016). In practice, the reference (pre-event) and target (post-event) point clouds are divided into tiles. Then, the 3D-deformation is determined by estimating a local rigid-body transformation between these tiles (i.e., translation and rotation), where for each point of the reference tile, the closest point in the target tile is computed. The rigid transformation is determined, by an iterative process, to minimize the square sum of the distance between the tangential plane of the reference point and its paired point in the target tile. The final local transformation is the cumulative rigid-body transformation determined at each iteration. In the case where we have pre-and post-rasterized DEMs, usually derived from a stereogrammetry process, we

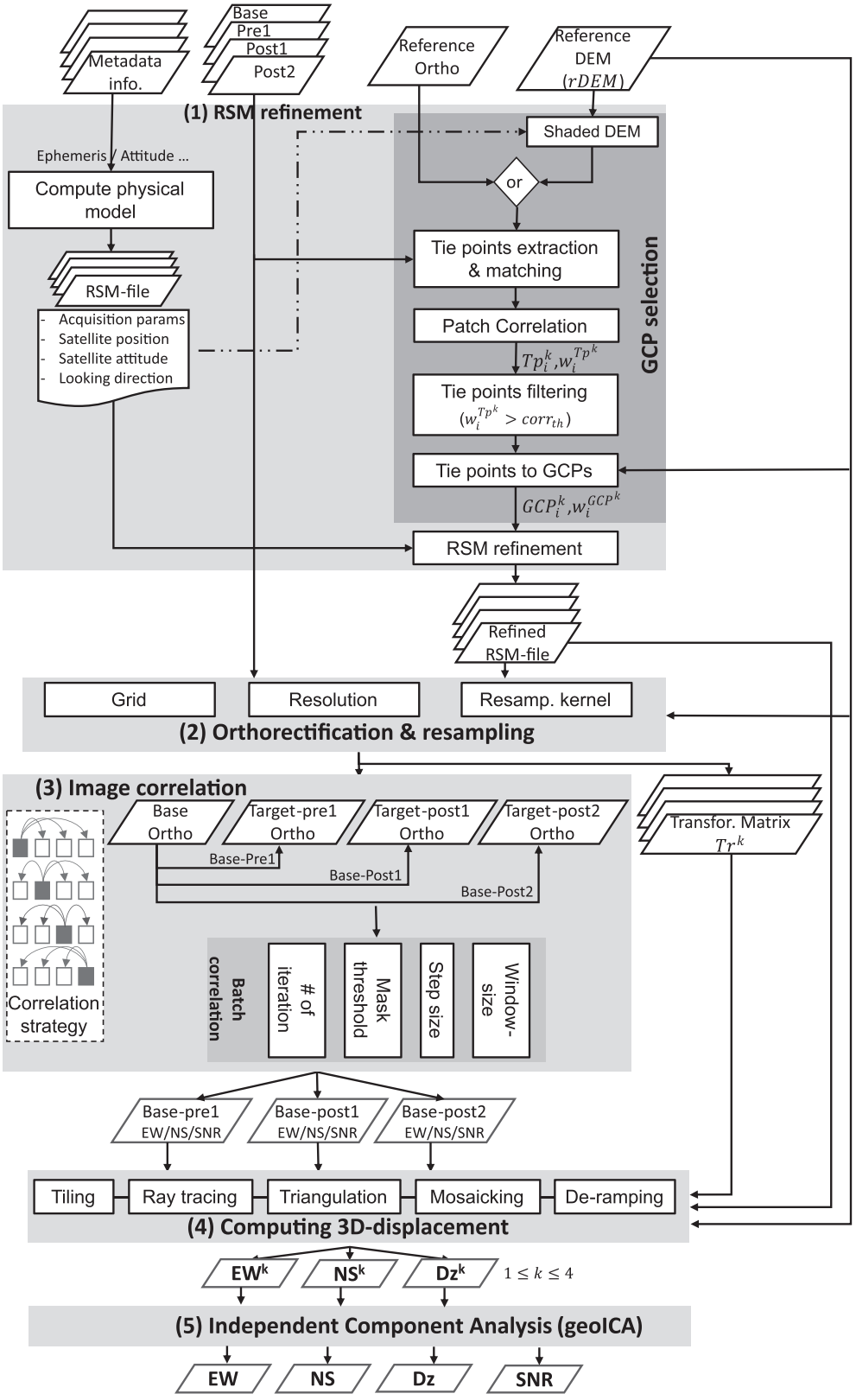

Fig. 2. Process flowchart of the proposed approach. The method comprises five stages: (1) Rigorous sensor model refinement (RSM), (2) Orthorectification and resampling, (3) Image correlation, (4) 3D-displacement calculation, and (5) Independent component analysis.

need to transform each raster to a regularly spaced point cloud at each tile center. The horizontal coordinates of each point are computed from the raster geo-transformation, and the vertical point coordinates are retrieved from the raster pixel value (Nissen et al., 2014).

The estimation of the local surface normal is a crucial step for the convergence of the ICP algorithm, which makes this approach very sensitive to outliers and very dependent on the qualities of the extracted DEMs (especially in the case of photogrammetry DEMs). Thus, filtering and smoothing the point cloud is required to properly estimate the local normal, which could lead to a loss of spatial resolution and details.

3. Proposed methodology

Here, we propose an alternative end-to-end workflow to extract high-quality surface deformation in 3D using multi-date and multi-platform high resolution (HR) optical imagery (Fig. 2). Part of the workflow uses the Co-registration of Optically Sensed Images and Correlation (COSI-Corr) methodology (Leprince et al., 2007), which was incorporated and augmented in a custom python/C++ freely accessible package referred to as COSI-Corr^{+} (geoCosiCorr3D). The software package allows: data preprocessing, physical geometry refinement, orthorectification, sub-pixel image correlation, 3D-displacement computation, and Geospatial Independent Component Analysis (geoICA). The COSI-Corr^{+} code repository accompanying this manuscript contains processing libraries and additional documentation of this workflow. In addition, we use the Ames Stereo Pipeline (ASP, version 2.7.0) for WorldView (WV) CCD correction (Beyer et al., 2018) and MicMac for tie point detection (Rupnik et al., 2017).

The set of input data required for our workflow includes the following:

- A set of four images spanning the event, which are referred to as "3D-set", one base image (pre-event), and three target images (pre-event, post-event1, and post-event2). The current package version supports raw images with the accompanying physical model metadata. So far, we have tested this approach only with off-nadir angle images >8°. However, it should be applicable too to data with smaller off-nadir angles, such as PlanetScope Doves images.
- A reference DEM referred to as "*rDEM*".
- Optional input: geo-referenced external image (e.g., HR aerial imagery)

In the case of a large number of images, automatic selecting of pairs could be performed, where additional inputs should be provided like the region of interest of the main event (e.g., the epicentral area in the case of coseismic deformation). The workflow output is a 4-bands geo-referenced displacement raster (East/West | North/South| Dz | residual).

The workflow consists of five processes (Fig. 2): (1) Rigorous sensor model refinement (RSM), (2) Orthorectification and resampling, (3) Sub-pixel image correlation, (4) 3D-displacement calculation, and (5) Filtering using the Independent Component Analysis. We detail these steps in the following sections.

3.1. Physical model refinement

Precise registration is essential to achieve a good quality displacement field. The most accurate approach involves a refinement of the image geometry through a rigorous sensor modeling (RSM) that provides the looking direction corresponding to each pixel corrected from the errors associated to the estimate of the satellite viewing parameters (e.g., spacecraft position, attitude variation, and the satellite's looking vector) (Leprince et al., 2007). The reader is referred to Aati and Avouac (2020) for a discussion of how RSM compares to other registration techniques. Therefore, satellite velocities, positions, attitudes, and sensor orientations are required to build the RSM. The metadata file does not have any standard format. The format of the RSM-file that describing the interpolated satellites position and attitude for each image line thus depends on the imaging system. Linear interpolation is used instead of Lagrange interpolation when the number of ephemeris and attitude data are provided at high frequency; moreover, throughout the interpolation process, the continuity and the global motion of the satellite are preserved.

The satellite positions are expressed in the WGS84 Earth-centered Earth Fixed (ECEF) Cartesian coordinate system. Additionally, the acquisition information is also stored in the same binary file (e.g., sun elevation/azimuth, satellite elevation/azimuth, off-nadir angle…). The rigorous sensor model relates the position of any point at the Earth surface relative to the center of the cartesian system (in this case Earth's center of mass), *O,* according to:

$$\overrightarrow{OM}(p) = \overrightarrow{OS}(p) + \lambda.\boldsymbol{T}(\boldsymbol{p}).\boldsymbol{R}(p).\overrightarrow{U}(p)\ , \tag{1}$$

where

- $M(p)$ is a point on the ground seen by the pixel p with coordinates [x, y],
- $S(p)$ is the position of the optical center in space when pixel p was being acquired,
- $\overrightarrow{U}(p)$ is the look direction vector of the pixel p, expressed in the satellite platform reference frame,
- $\boldsymbol{R}(p)$ is the 3D-rotation matrix that accounts for the satellite roll, pitch, and yaw when p was being acquired,
- $\boldsymbol{T}(\boldsymbol{p})$ is the transformation matrix to go from the platform to the terrestrial coordinate system,
- λ denote the scaling factor determined from the intersection of the ray with the Earth ellipsoid.

Note that bold symbols refer to matrices.

In our approach, the look directions of the imaging system are refined globally by adding a correcting term $\overrightarrow{\delta}(p)$ to the physical model using a set of GCPs and expressed in ECEF coordinate system. This correction compensates globally for satellite jitter due to the pitch, roll, and yaw variations along the satellite trajectory and aberrations from the imaging system. The correction is defined as:

$$\overrightarrow{OM}_{corr}(p) = \overrightarrow{OS}(\mathrm{p}) + \lambda.\left[\boldsymbol{T}.\boldsymbol{R}(p).\overrightarrow{U}(p) + \overrightarrow{\delta}(p)\right], \tag{2}$$

$$\overrightarrow{\delta}(p) = \boldsymbol{A}\begin{bmatrix} x \\ y \\ 1 \end{bmatrix}. \tag{3}$$

where $\boldsymbol{A}$ is a 3 × 3 matrix and $[x, y, 1]^{T}$is the homogeneous coordinate vector of the pixel p.The correction matrix $\boldsymbol{A}$ is determined by using a Weighted Least Squares criterion with a stochastic model computed using a weight assigned to each GCP. The correction $\overrightarrow{\delta}(p)$ accounts for the drift of the satellite attitude and the nonlinear distortion due to the local topography. Next, a refined RSM-file that includes this correction is generated for each input image.

This approach is different from the one described in (Leprince et al., 2007) and currently implemented in the COSI-Corr software, where instead of optimizing the viewing parameters of a given set of GCPs, a new set of GCPs is estimated by correcting the ground coordinates of each GCP using the ground offset found between a reference and target orthorectified patches at each GCP location. One key advantage of our approach is that it makes bundle adjustment possible, therefore allowing to refine multiple images at the same time.

In-situ measurement of a clearly identifiable feature on the image, a common practice to define control points, is expensive and may not be applicable depending on the accessibility of the area. In our workflow, the GCPs are extracted automatically. First, based on feature detection, tie points are selected between each raw image of the input *3D-set* and an

Table 1
Example of the correlation parameters used in this study.

Parameters	Values
Initial window size [pixel]	128 × 128
Final window size [pixel]	32 × 32
Step size [pixel]	8 × 8
Iteration	2
Mask threshold	0.9
Grid	True
Correlation strategy	Full

already orthorectified reference image (e.g., HR aerial images). These points are filtered and weighted using a frequency correlation technique in image space. The weight of each GCPs corresponds to the Signal to Noise Ratio (SNR) of the correlation $w_i = SNR_i$, while GCPs with SNR score under a predefined threshold are discarded. The correlation results are retrieved between two patches (base and target) centered on the pixel coordinates of the reference and raw image, respectively. Then, the tie points are converted to GCPs, where the georeferencing of the reference image provides the horizontal coordinates, while the elevation is interpolated from the *rDEM*.

If no external data is available, a shaded DEM relief map is constructed with lighting corresponding to the sun azimuth and elevation angles at the time of the acquisition of each input image. The sun elevation and azimuth are extracted from the generated RSM-file, and the shaded DEM provides both horizontal and vertical coordinates. In this case, the location of the selected GCPs is very inaccurate, thus optimizing the GCPs with the original approach of COSI-Corr is recommended (Leprince et al., 2007).

3.2. Orthorectification and resampling

All the *3D-set* images are orthorectified to the same resolution and with elevation information from the *rDEM*. In this step, the images are resampled to correct for the long-wavelength stereo component that occurs because of the stereoscopic effect produced when images are acquired at wide off-nadir angle. The images are orthorectified on a UTM grid to provide a support independent of the acquisition system and to allow pairing images from different platforms (e.g., push-broom, push-frame, or frame).

The inverse orthorectification model is used, in which we determine for each grid element the non-integer pixel coordinates in the raw image by exploiting information from the refined RSM-files.

The inverse orthorectification model is defined as:

$$[x, y] = argmin_{x,y}\Omega(x, y), \tag{4}$$

$$\Omega(x, y) = \left\|\overrightarrow{OM} - \overrightarrow{OM'}\right\|_2^2, \tag{5}$$

where (x,y) are the pixel coordinates in the raw image associated with point M in the projection grid and M' is the point projected onto the ground using the refined RSM.

The output of the inversion is stored into a 2-band raster array $\boldsymbol{Tr}$ of the same dimension as the orthorectification grid. Band-1 and band-2 correspond respectively to the 2D matrices of $\boldsymbol{X}(x_{pix}, y_{pix})$ and $\boldsymbol{Y}(x_{pix}, y_{pix})$ coordinates of the pixel $p(x_{pix}, y_{pix})$ in the raw image to be projected. Ultimately, the orthorectified images are constructed by resampling the raw images according to the transformation matrices. To minimize resampling biases, a sine cardinal kernel (15 × 15 pixels) is used for the resampling process.

3.3. Image correlation

This step consists in selecting a base image and correlate with the other *3D-set* images. Consequently, three horizontal displacement maps ($\boldsymbol{corr}^j, j \in \{1..3\}$) are derived. Ideally, all image pairs should be correlated so that no one image is given more weight than the others. Therefore, the option to progressively apply j independent correlations is possible (Fig. 2). When selected, correlations are applied iteratively using all available images in the *3D-set* as the base, thus achieving a redundant stack of horizontal displacement maps ($\boldsymbol{corr}^j, j \in \{1..12\}$).

The horizontal offsets are retrieved iteratively in two steps by applying a multi-scale sliding window. An initial window size maximizes the correlation between the base and target images, while a smaller final window size provides a finer offset estimation. The correlations are processed using the frequency correlator implemented in COSI-Corr$^+$, which is based on the principle that a translation in space corresponds to a phase shift in the frequency domain. Other correlation approaches, such as multi-scale normalized cross-correlation (NCC), can also be applied. Here, we chose to perform the correlation in the frequency domain because it can achieve 1/20-pixel accuracy (Leprince et al., 2007) and is faster than the spatial correlators, which is very important if we are processing a large data cube of images.

Several parameters must be selected to perform the correlation, including initial and final window sizes, step size, number of iterations, and the mask threshold. The specific parameters for the correlation used in this study are listed in Table 1.

Each correlation provides a 2-D offset vector map, that should correspond directly to horizontal displacements along the East-West (E/W) and North-South (N/S) directions and a signal-to-noise ratio (SNR, ranging from 0 to 1), which assess the measurement quality. The components of the offsets/displacements vectors are measured positive eastwards and northwards. To automate the correlation process, a batch correlation is used.

The pre-event (Base-pre1) offset map reflects only the topographic stereo disparities remaining in the pre-ortho images, which is small enough to be measured with the frequency correlator, thus because no deformation is present in the pre-event "base-pre1" correlation ($\boldsymbol{corr}^{j=1}$). Whereas the two post-event correlations, "base-post1" and "base-post2", contain both the ground displacement signal and the stereoscopic offsets.

3.4. Computing 3D-displacement

Computing the 3D displacement field involves the following steps:

(1) Cropping the j−correlations maps to the same extent and discarding the displacement values with low SNR values.
(2) Tiling the *rDEM*, correlations ($\boldsymbol{corr}^j$, $3 \leq j \leq 12$) and transformation matrices ($\boldsymbol{Tr}^k$, $k \in \{1..4\}$) into raster blocks (default 256 × 256 pixels) for parallel processing.
(3) Computing for each pixel $p(x_{pix}, y_{pix})$ in the correlation map ($\boldsymbol{corr}^j$) the ray vector relating the satellite position with the ground position. This is accomplished by combining the spacecraft refined RSM information (i.e., ephemeris/attitude) and the correlation offsets. First, latitude and longitude are extracted directly from the correlations ($\boldsymbol{corr}^j$), while elevation ($elev^k$) is interpolated from the *rDEM*. Second, the ground position P^k_{ECEF} is computed by converting the geographic coordinates in a Cartesian Earth-Centered Earth-Fixed (ECEF) coordinate system. Third, the satellite position P^k_{satPos} of pixel p is determined by combining the refined satellite position ($eph.\ satPos^k$) and the orthorectification inverse transformation ($\boldsymbol{Tr}^k$). Finally, the sight-vector $S^k_{(p)}$ is given by the difference between ground P^k_{ECEF} and satellite P^k_{satPos} positions.
(4) Triangulating the 3D-ground position at each pixel location p before (P^{pre}) and after (P^{post}) the event. The triangulation routine (*geoTriangulte*) computes the 3D coordinates in ECEF coordinate system for the closest intersection, first between the two pre-event sight vectors ($S^{k=1}_{(p)}$, $S^{k=2}_{(p)}$), and then separately between the post-event sight vectors ($S^{k=3}_{(p)}$, $S^{k=4}_{(p)}$). The full 3D-

Inputs:
- Reference DEM $rDEM$
- Inverse ortho -transformations $Tr^k, k \in \{1..4\}$
- Refined RSM -files, , $k \in \{1..4\}$
- Correlation $corr_j, j \in \{1..3\}$; 1: base -pre1, 2: base -post1 ,3: base-post2

Output : 3D-Displacement raster

Cropping $corr_j$ to the same extent;
Discard pixels with $SNR^j < th$;
for $p = (x_{pix}, y_{pix}) \in corr_j$ **do**
  $(X,Y)^{k=1}_{map} \leftarrow T^{corr\ 1}.p$;
  $(X,Y)^{k}_{map} \leftarrow (X,Y)^{k=1}_{map} + (ew(p), ns(p))^{corr\ j}$; $\{(k,j) = (2,1),(3,2),(4,3)\}$
  $elev^{k} \leftarrow Interp2D\left(rDEM, T^{-1}_{rDEM}.(X,Y)^{k}_{map}\right)$;
  $P^{k}_{ECEF} \leftarrow Conv2Cart\left((X,Y,elev)^{k}_{map}\right)$;
  // Compute sight vectors
  $ephem.satPos^{k} \leftarrow RSMfile^{k}$;
  $P^{k}_{satPos} \leftarrow Interp1D\ (ephem.satPos^{k}, Interp2D\ (Tr^{k}, Tr^{-1}.(X,Y)^{k}_{map}))$;
  $S^{k}_{(p)} \leftarrow P^{k}_{satPos} - P^{k}_{ECEF}$;
  //Triangulation
  $resi^{pre}, P^{pre} \leftarrow Triangulate\left(l1:(P^{k=1}_{ECEF}, S^{k=1}), l2:(P^{k=2}_{ECEF}, S^{k=2})\right)$;
  $resi^{post}, P^{post} \leftarrow Triangulate\left(l3:(P^{k=3}_{ECEF}, S^{k=3}), l4:(P^{k=4}_{ECEF}, S^{k=4})\right)$;
  $(ew_{(p)}, ns_{(p)}, dz_{(p)}) \leftarrow P^{post} - P^{pre}$;
return $ew, ns, dz, resi^{pre}, resi^{post}$;

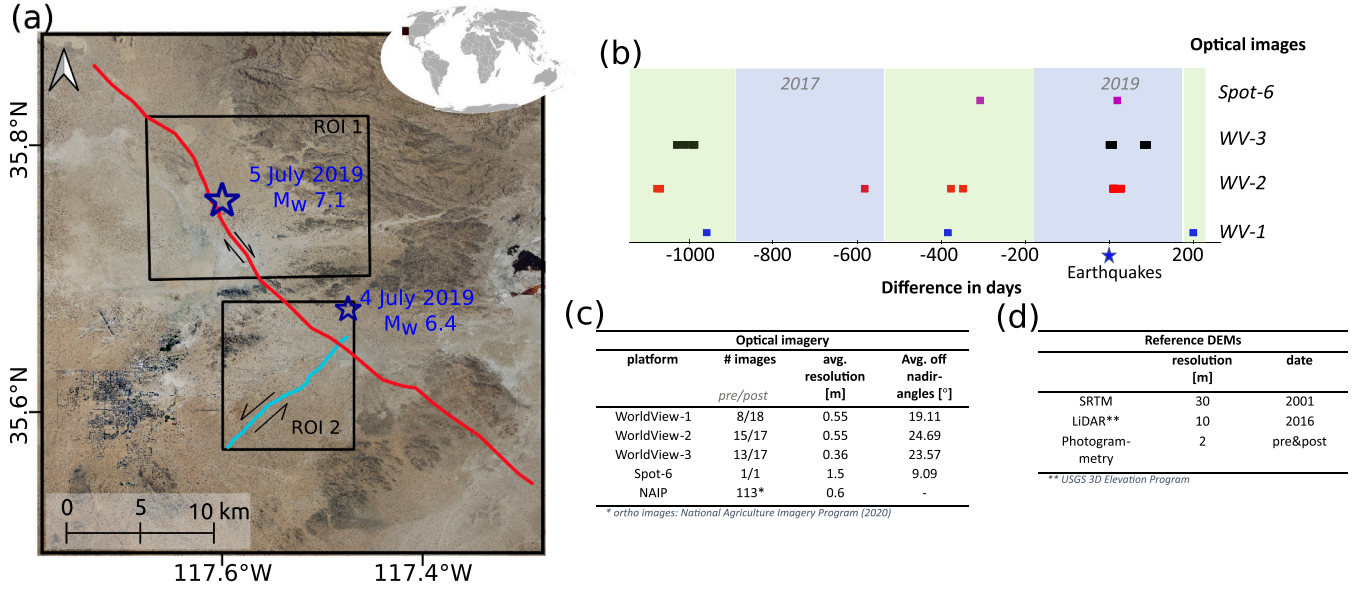

(c)

Optical imagery			
platform	# images pre/post	avg. resolution [m]	Avg. off nadir-angles [°]
WorldView-1	8/18	0.55	19.11
WorldView-2	15/17	0.55	24.69
WorldView-3	13/17	0.36	23.57
Spot-6	1/1	1.5	9.09
NAIP	113*	0.6	-

* ortho images: National Agriculture Imagery Program (2020)

(d)

Reference DEMs		
	resolution [m]	date
SRTM	30	2001
LiDAR**	10	2016
Photogram-metry	2	pre&post

** USGS 3D Elevation Program

Fig. 3. Overview of the study area and used datasets. (a) The inset shows the geographic location of the study area with a true-colour NAIP image as background. A simplified rupture map of the M_w6.7 occurred on July 4, 2019, in a cyan polyline, and the M_w7.1 occurred on July 5, 2019, in a red polyline. The black rectangles represent the selected region of interest. (b)Timeline of the satellite images used in this study with respect to the date of earthquakes. (c,d) Key characteristics of image datasets and digital elevation models, respectively used in this study. (For interpretation of the references to colour in this figure legend, the reader is referred to the web version of this article.)

displacement vector is then estimated at each pixel location p by the difference between the triangulated pre (P^{pre}) and post (P^{post}) event positions. The output is a 5-band raster file format, with the same projection system as the ortho-images. Band-1 contains the E/W displacement ($\boldsymbol{ew}_{(p)}$), band-2 the N/S displacement ($\boldsymbol{ns}_{(p)}$) and band-3 the vertical displacement ($\boldsymbol{dz}_{(p)}$), band-4 and -5 provide, respectively, normalized triangulation errors for the pre- and post-event ortho-images. These errors are mainly the horizontal disparities not resolved during the orthorectification process and the remaining or unmodeled artifacts (e.g., CCD misalignment and jitter).

(5) Merging all the tiles to build the final 3-D displacement map.
(6) De-Ramping: the displacement retrieved after the correlation and triangulation contain long-wavelength errors related to the selected GCPs used for the RSM refinement. Given the small swath of the input images, the single date reference DEM and

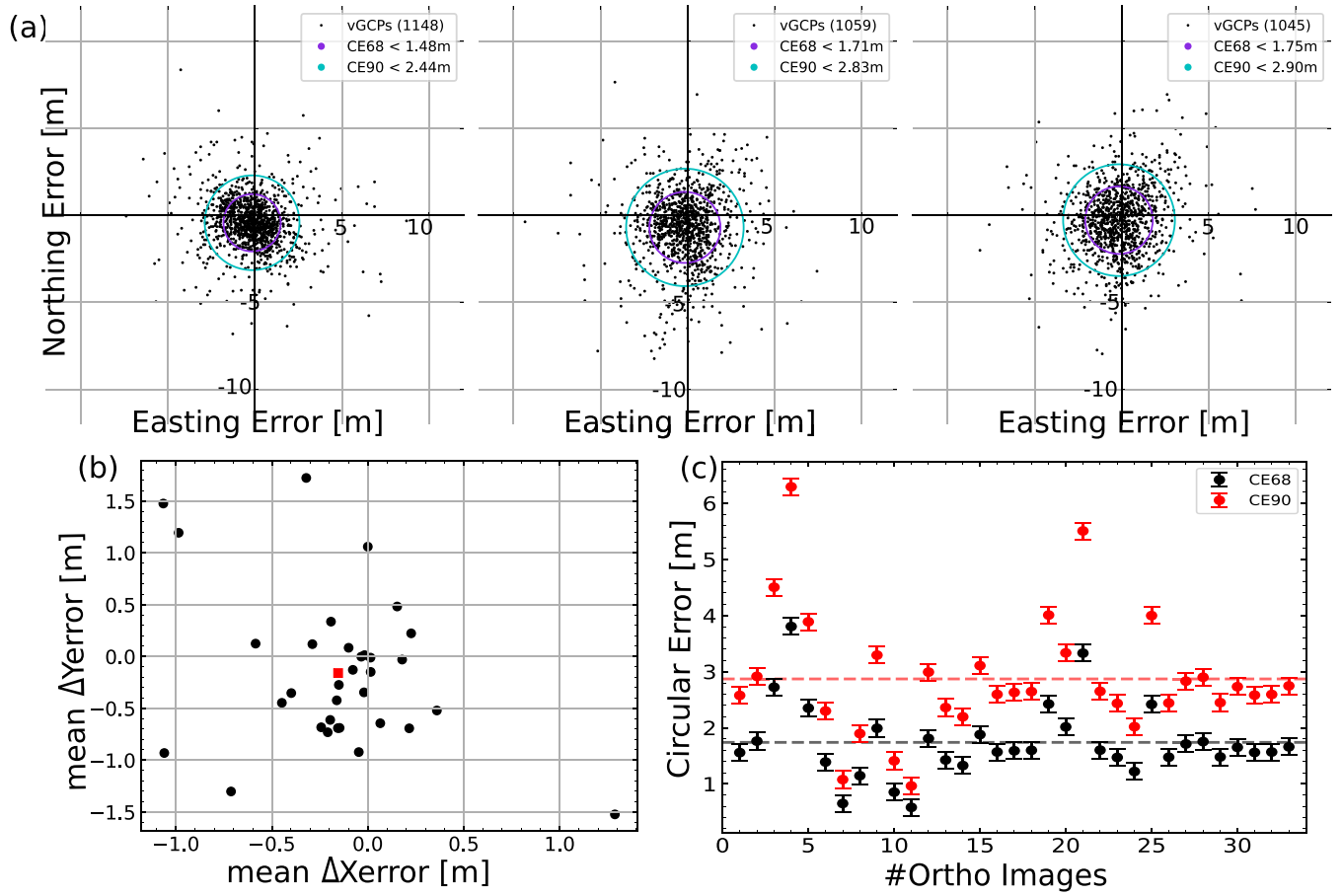

Fig. 4. Co-registration assessment. (a) Example of measured horizontal geolocation errors (in meter) of an orthorectified WV-1 image acquired on June 16, 2018. Three ortho-images were generated at 60 cm GSD using three rDEMs: Pre-DEM (left), Lidar (center), and SRTM (right). Scatterplots show the 2-D misregistration shifts in-ground space (UTM-11 N). The purple and cyan circles indicate 68CE and 90CE, respectively. The black points represent the extracted vCPs between the ortho-images and the ref-image (NAIP). (b) Registration uncertainty, each black point represents the average X-shift and Y-shift measured in each ortho-image with respect to the ref-image. The red square represents the average registration value of all ortho-images (ΔX, ΔY) = (− 0.1, − 0.2) m. (c) Circular errors 68CE (black) and 90CE (red) of the 34-ortho-images. The error bars show the mean values of the biases (shift) in X and Y. The horizontal dashed black (68CE) and Red (90CE) lines indicate the mean circular error of all ortho-images (k = 33), respectively. A summary of all computed statistical values is reported in Table S.2. (For interpretation of the references to colour in this figure legend, the reader is referred to the web version of this article.)

Table 2
Summary of horizontal geolocation accuracy results and errors for the generated ortho-images after RSM-refinement. (Complete table provided in Table S.2).

	# ortho	Mean 68CE	Mean 90CE	Mean RMSExy	Mean stdxy
All ortho	33	1.74	2.87	1.93	1.82
Ortho images – *rDEM*					
Lidar	21	1.41	2.33	2.29	2.22
SRTM	4	3.07	5.08	4.76	4.47
Pre-Post	7	1.40	2.34	2.26	2.09
Ortho images – resolution					
GSD (60 cm)	27	1.49	2.47	2.35	2.26
GSD (1.5 m)	6	2.84	4.70	4.40	4.20
Ortho images – Off-Nadir angle					
<10°	3	0.70	1.15	1.08	1.07
10°-15°	5	1.32	2.18	2.05	2.02
15°-25°	9	1.57	2.59	2.38	2.29
>25°	16	2.16	3.64	3.44	3.26

reference ortho-image, it is difficult to avoid the effect of the displacement on the selected GCPs. Therefore, the long-wavelength error is modeled by estimating the parameters of 2D affine transformation denoted in Eq.(6). The unknown parameters are estimated using an iteratively reweighted least squares (IRLS) criterion with a bi-square loss function minimizing the residuals between the measured and modeled offsets (Holland and Welsch, 1977; Stumpf et al., 2018). Displacements from modeled error are then subtracted from the initial computed displacement maps.

$$u^{d}_{x,y} = a_1 x + a_2 y + a_{13}\ , \tag{6}$$

where $u^{d}_{r,c}$ is the displacement value of the pixel $p(x,y)$ with respect to the displacement map $d \in \{EW, NS, Dz\}$ and a_1, a_2, a_3 are the unknown parameters.

Algorithm 1. 3D-Displacement computing algorithm.

3.5. Geospatial Independent component analysis (geoICA)

The 3D displacement map obtained using a single correlation strategy (i.e., selecting a base image then correlating it with the three target images) includes the surface deformation signal and other artifacts, such as the CCD stripe artifacts, satellite jitter, outliers, topographic residuals, and decorrelation noise. The artifacts due to the CCD misalignment and jitter, can in principle be estimated and corrected, but the current methods require an accurate calibration site and precise GCPs (Ayoub et al., 2008; Jiang et al., 2018; Leprince et al., 2008; Tong et al., 2015; Ye

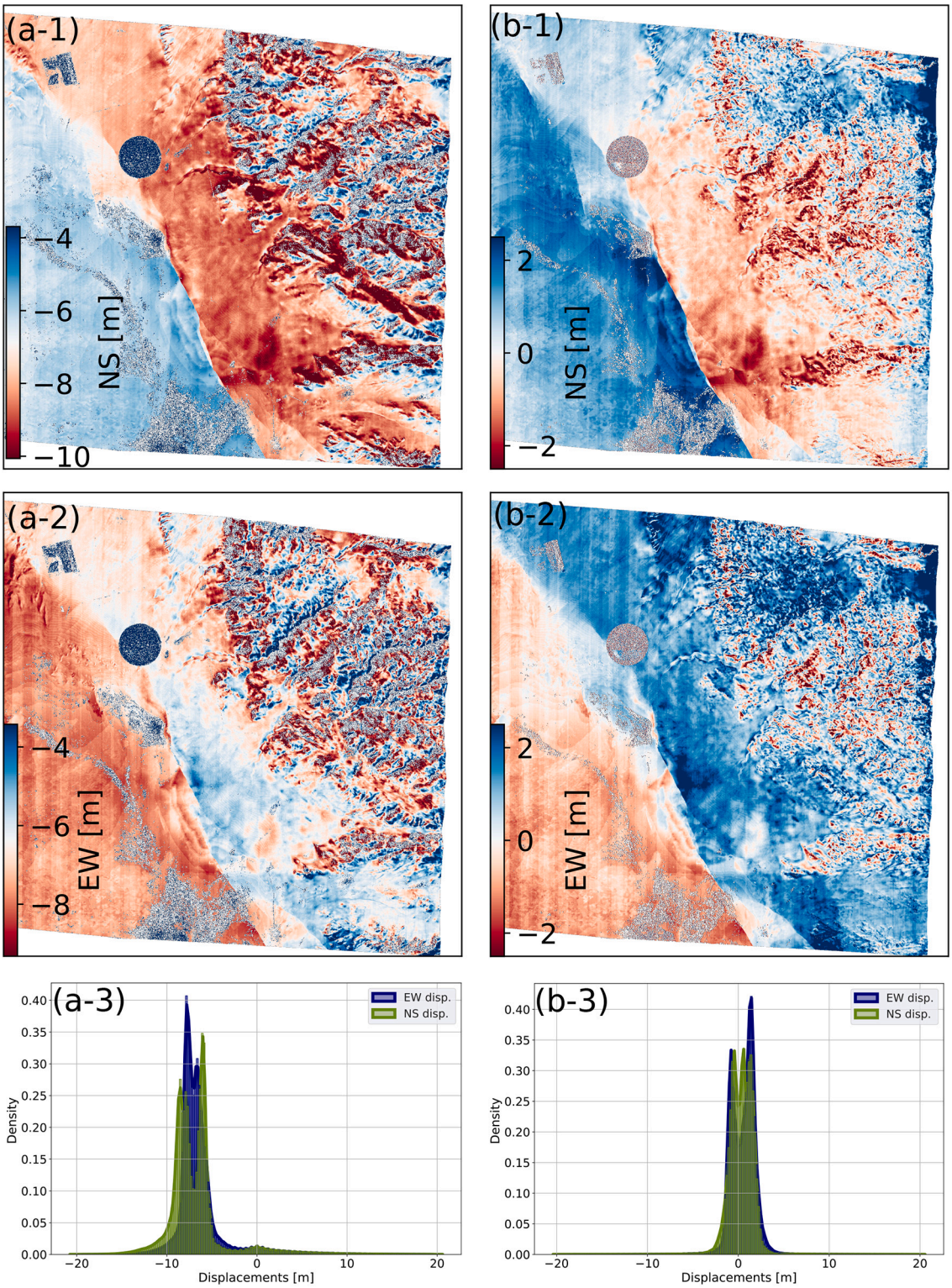

Fig. 5. RSM refinement assessment. Column (a) corresponds to the correlation results between pre-and post-earthquake WV-2 orthoimages acquired on June 23, 2018, and July 14, 2019, respectively, and orthorectified with the state-of-the-art method. Column (b) corresponds to the correlation results using the same orthorectified images processed with our method. (a-1,b-1) the N-S displacements, (a-2,b-2) the *E*-W displacements and (a-3,b-3) displacements density distributions.

et al., 2020). These methods were developed to compensate for the geometric artifacts of a specific imaging system and are not easily applicable when data from newly available systems are used. Our ICA-based approach has the advantage to be more general and sensor agnostic.

To reduce the effect of these artifacts, we resort to an Independent Component Analysis. An ICA decomposition is used rather than a Principal Component Analysis (PCA) because the sources of artifacts can be a major contribution to the data variance and could be filtered out by selecting only the first component of a PCA. The basis for the decomposition is that the deformation signal and the various sources of artifacts can be assumed to be statistically independent sources. In

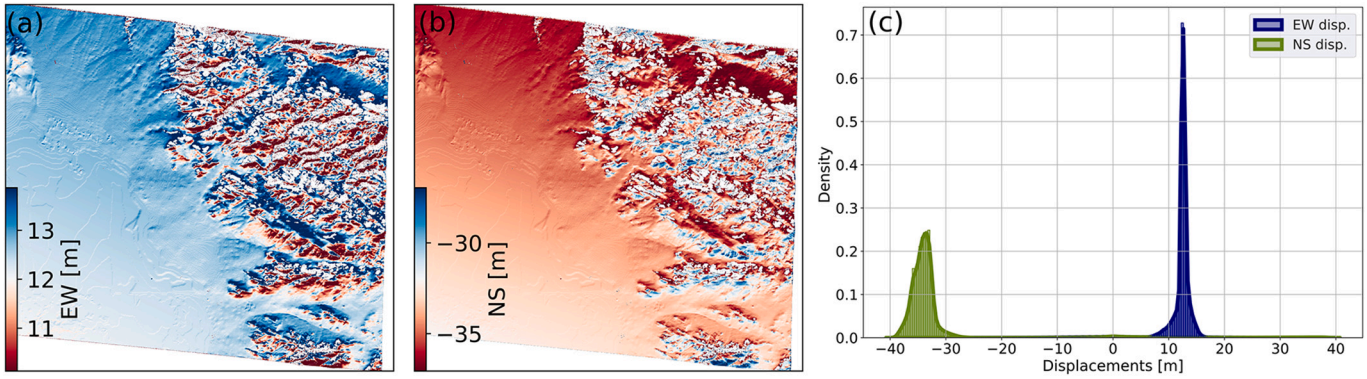

Fig. 6. RSM refinement impact. Maps of EW (a) and NS (b) displacements and density distributions (c) measured by correlating a WV2 image orthorectified with RPC-based method and the same image orthorectified with our method. The image was acquired on July 14, 2019. The values of the correction matrix A estimated for the RSM refinement are: −1.072e-11 5.803e-11 3.3574e-11 7.809e-11 -1.254e-11 -3.862e-11 -1.613e-05 1.046e-05 1.118e-05.

particular, the artifacts are assumed to be statistically independent with the deformation signal. The deformation signal is presumed to be the same in all the 3-D measurements maps independent of the choice of a particular set of images. As a result, we expect the deformation signal to show in only one component. The hypothesis that the displacement signal is independent of the artifacts is most likely to be verified in real applications. This assumption would be incorrect only in the unlikely case of a displacement signal similar with the pattern resulting from jitter or CCD artifacts.

We implemented a modified version of the FastICA algorithm (Hyvärinen and Oja, 2000; Shlens, 2014), which is included in the COSI-Corr^{+} package, this routine version referred to as Geospatial ICA (*geoICA*).

This approach can be considered as unsupervised learning and can be summarized as follows:

(1) The overlapping displacements maps are cropped to the same extent and stored in the data cube $\boldsymbol{X^d}$,where $\boldsymbol{d}$ represents the displacement directions (EW, NS, and Dz).
(2) The outliers in the decorrelation areas are filtered out, then the "no data" values mask is constructed and applied to $\boldsymbol{X^d}$.
(3) Assuming that $\boldsymbol{X^d}$ is a linear combination of m independent sources $\boldsymbol{S}$. The data cube is expressed as $\boldsymbol{X^d} = \boldsymbol{A.S}$, where $\boldsymbol{A}$ is the mixing matrix and $\boldsymbol{S} = \sum_{i=1}^{m} \boldsymbol{s_i}$, with $\boldsymbol{s_i}$ are the sources and $\boldsymbol{m}$ the number of sources. If there are 4 input images, the number of observations using the progressive correlation strategy is $\boldsymbol{n} = 4$, then $\boldsymbol{m} \leq \boldsymbol{n}$. In our case, we assume that the sources are displacement and artifacts (i.e., $\boldsymbol{S} = \boldsymbol{d} + \boldsymbol{B}_{k \leq m-1}$, where $\boldsymbol{B}_{k \leq m-1}$ represents the different sources of artifacts). The sources are recovered by determining the unmixing matrix $\boldsymbol{A}^{-1}$, which is performed in two successive stages:
   a. Whiten the data by calculating the eigenvectors of the covariance of $\boldsymbol{X^d}$, to remove all linear dependencies (i.e., decorrelate the data) in the dataset and normalize the variance,
   b. Assume the statistical independence of the sources. The joint probability density function (pdf) of the sources, is denoted $\mathfrak{p}(s_1, s_2, \ldots, s_n) = \prod_{i=1}^{n} \mathfrak{p}(s_i)$, where $\mathfrak{p}(s_i)$ is the probability density function of source s_i. The matrix is computed using an iterative process that maximizes the non-gaussianity of the whitened data sets using a contrast function G that approximate the negentropy. G is defined as $G(u) = -\frac{e^{-au^2_2}}{a}$, where a is user-defined constant.
(4) The source which is identified to represent the displacement signal is used to reconstruct n-displacement maps, which then are stacked by average to yield the final displacement result.
(5) The measurement uncertainty is quantified from the residuals with our best estimate of the signal derived from combining all the measurements derived from the 90 images used in this study.

4. Study area and datasets

4.1. Study area

The performance of the methodology described above to measure the three-dimensional surface-displacement field is demonstrated using the Ridgecrest earthquake sequence, which occurred in California in 2019. The two dominant events, a M_w 6.4 foreshock event on July 4th (a left-lateral strike-slip rupture) followed 34 h later by a M_w 7.1 mainshock event on July 5th (a right-lateral strike-slip rupture), were felt over most of southern California and caused surface ruptures with minor damage to infrastructure. The region of interest spans over an area of ~1864 km^2, consisting mostly of desert and rugged terrain with elevations between 500 m to 1500 m (Fig. 3). This region is particularly well suited for remote sensing observations of ground deformation using optical images and the technique has therefore been used in several previous studies (Antoine et al., 2021; Barnhart et al., 2020; Chen et al., 2020; Milliner et al., 2021). The M_w 7.1 mainshock produced right-lateral surface ruptures extending over ~50 km along a northwest direction, and the M_w 6.4 foreshock produced left-lateral surface ruptures with a southwest trend over ~14-km-long (Fig. 3).

For the purpose of illustrating our results, we selected two sub-regions. The first sub-region (ROI-1), located in the upper north-western part of the M_w 7.1 surface ruptures, covers an area of ~231 km^2. The second sub-region (ROI-2) covers the M_w 6.4 surface ruptures, with an area of ~99 km^2.

Only the result from ROI-1 are presented and discussed in the main manuscript. The results for ROI-2 and the entire study area are provided as supplement.

4.2. Datasets

We used a total of 90 HR satellite optical images out of which 37 were acquired before the earthquake and 53 after. The pre-earthquake images were collected between the 23rd of July 2016 and the 1st of September 2018, and the post-earthquakes images between the 6th of July 2019 and the 21st of January 2020. They were acquired by the Spot-6, WorldView-1 (WV1), WorldView-2 (WV2) and WorldView-3 (WV3) satellites with nominal pixel resolutions of 1.5 m, 0.46 m, 0.46 m and 0.31 m, respectively. The images used in this study and their characteristics are listed in Table S.1. For our analyses only panchromatic band were used.

We used three different DEMs to assess the sensitivity to the

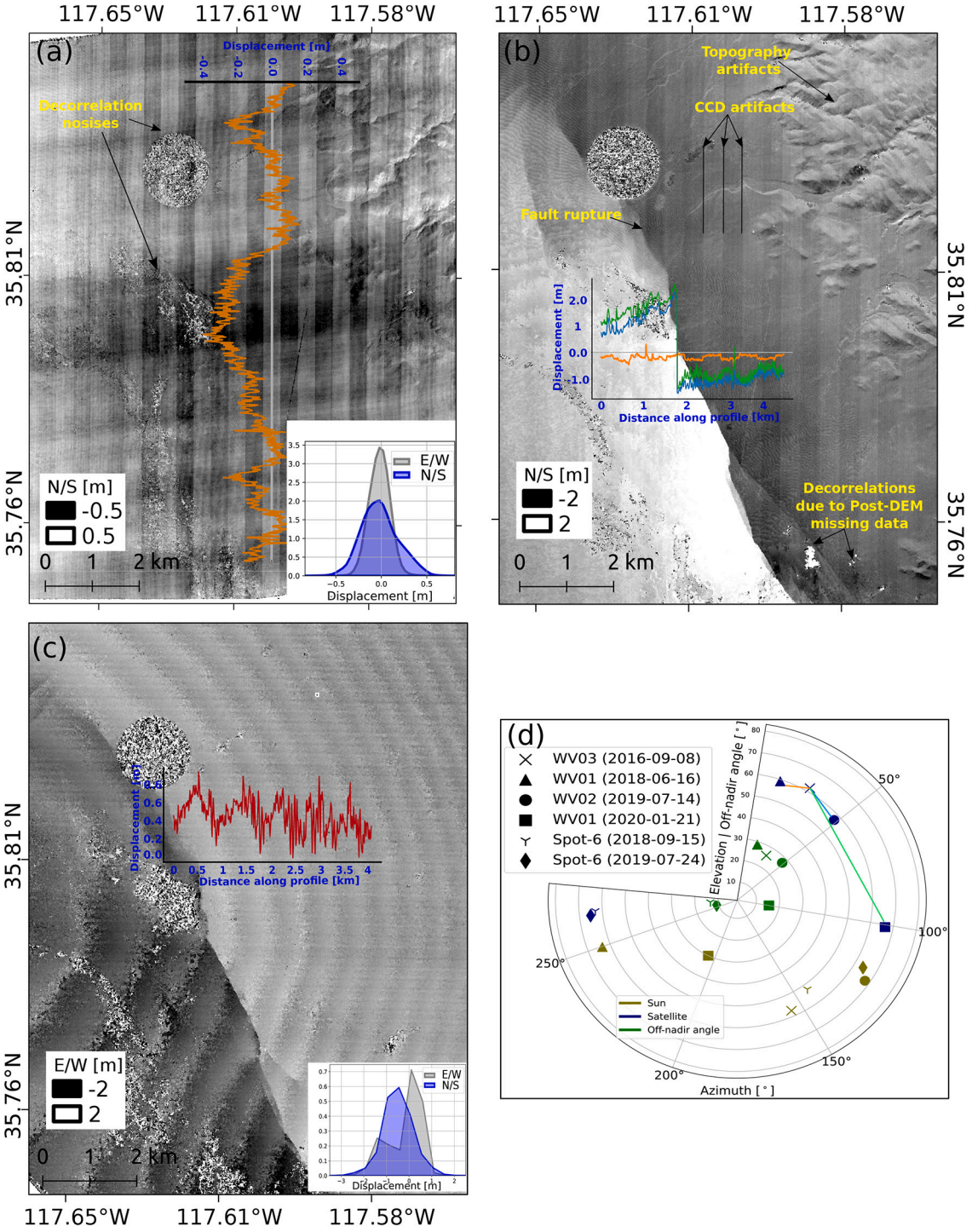

Fig. 7. Image geometric artifacts induced in correlation maps. (a) North/South component (northward positive) of the displacement map computed between two pre-event images (WV-3 acquisition from September 08, 2016, and WV-2 acquisition from June 16, 2018). No measurement is assigned to white points where the correlation is too weak. The superimposed graph shows the bias included by the jitter artifact. **(b)** North/South component map of the M_w 7.1 coseismic displacement field due to the 2019 Ridgecrest earthquake. The pre-earthquake image (WV-3) and the post-earthquake image (WV-2 acquisition from July 14, 2019) were resampled and orthorectified at 60 cm resolution on a 2 m pre- and post-DEMs, respectively. The offsets were measured from a sub-pixel correlation between a multi-scale sliding window of 128 × 128 to 64 × 64 pixels, sliding with a step of 8 pixels. The superimposed graph shows the N/S displacement within this box. The orange profile estimates the bias included by the CCD distortions of both WV-3 and WV-1 images before the earthquake. Blue and orange profiles estimate the displacement between images bracketing the earthquake. **(c)** E/W component (Eastward positive) over the same area between two Spot-6 images bracketing the earthquake. The fault rupture is identifiable, but the measurement is biased due to the aliasing artifacts. The red profile estimates the amplitude of the aliasing. **(d)** Skyplot with satellite azimuth and elevation angles in blue for the different H.R. images. In olive, the azimuth and elevation of the sun the time of acquisition. In green, the off-nadir angle. A specific symbol characterizes each satellite. Green, blue, and orange baselines correspond to the correlation pairs used for profiles in panel (a). (For interpretation of the references to colour in this figure legend, the reader is referred to the web version of this article.)

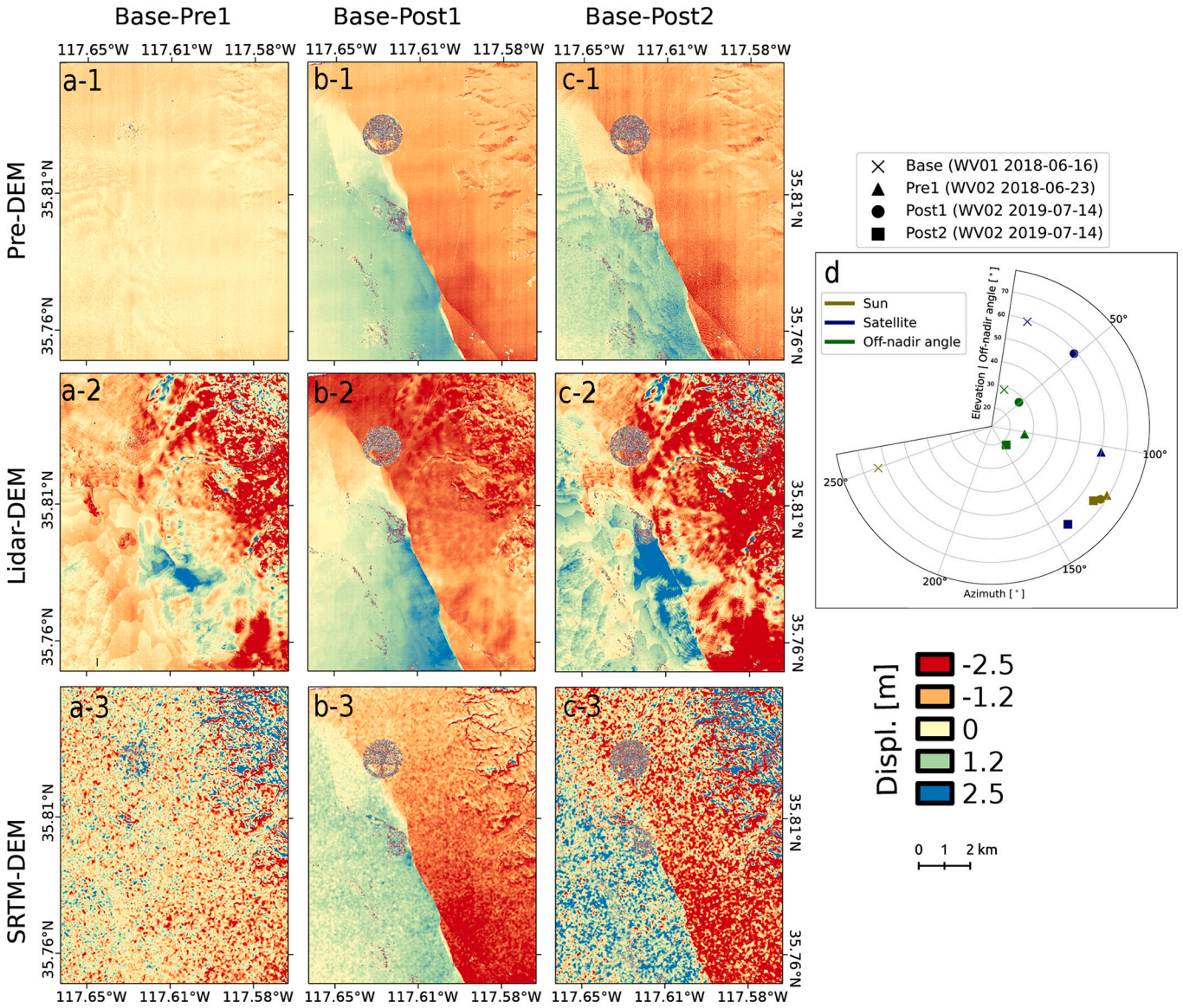

Fig. 8. N/S component of the horizontal displacement. The Base-Pre1 column **(a)** corresponds to the correlation between two pre-event images (WV1 and WV2 images acquired on June 16, 2018, and June 23, 2018, respectively). Base-post1 **(b)** and Base-post2 **(c)** columns correspond to the correlation of two images bracketing the M_W 7.1 earthquake. WV1 as the pre-event image and the stereo pair WV2 as the post-event images (the stereo-images were acquired on July 14, 2019). The images were orthorectified and resampled to 60 cm resolution using three different DEMs: pre-DEM (1 m), Lidar DEM (10 m), and SRTM DEM (30 m). **(d)** Skyplot with satellites: azimuth, elevation, and off-nadir angles and the position of the sun.

reference DEM used as input (*rDEM*): (1) the 30-m resolution DEM from the Shuttle Radar Topography Mission (SRTM), which was collected using radar (C-band) interferometry in February 2000 (Farr et al., 2007), (2) the 10-m publicly available airborne LiDAR data (hereafter referred to as "LiDAR DEM") collected over Ridgecrest in 2016 and accessed from Open Topography (www.opentopography.org), June 2020,(3) pre-and post-event photogrammetric DEMs with a resolution of 2 m, referred to as (Pre-DEM and Post-DEM), which we generated from in-track stereo pair acquired in July 2016 and July 2019, respectively.

Furthermore, 113 orthorectified aerial photos with a resolution of 60-cm were used as reference images to extract GCPs and to assess the horizontal geolocation accuracy of the orthorectified satellite images. The aerial photos were acquired between July 22 and September 01, 2018 and are publicly available through the National Agriculture Imagery Program (NAIP).

5. Results

5.1. Accuracy assessment

5.1.1. RSM refinement and co-registration accuracy

In this section, we assess the overall 2D geolocation accuracy of the ortho-images generated with refining the RSM using a well geolocalized reference image (*ref-image*). 16 raw images were orthorectified: WV1 ($n = 4$), WV2 ($n = 7$), WV3 ($n = 3$) and Spot-6 ($n = 2$) using the workflow outlined in Section 3. A total of 34 ($k = 34$) orthorectified image were generated with a ground sampling distance of 60 cm ($n = 28$) and 1.5 m ($n = 6$), using three different *rDEMs*: Pre/Post photogrammetry DEM ($n = 7$), LiDAR-DEM ($n = 23$) and SRTM-DEM ($n = 4$).

The evaluation was performed using a well-matched set of tie points between the *ref-image* (NAIP) and the *3D-set* generated ortho-images. Tie points were extracted using Scale-Invariant Feature Transform (SIFT) (Lowe, 2004), then refined using the image correlation procedure

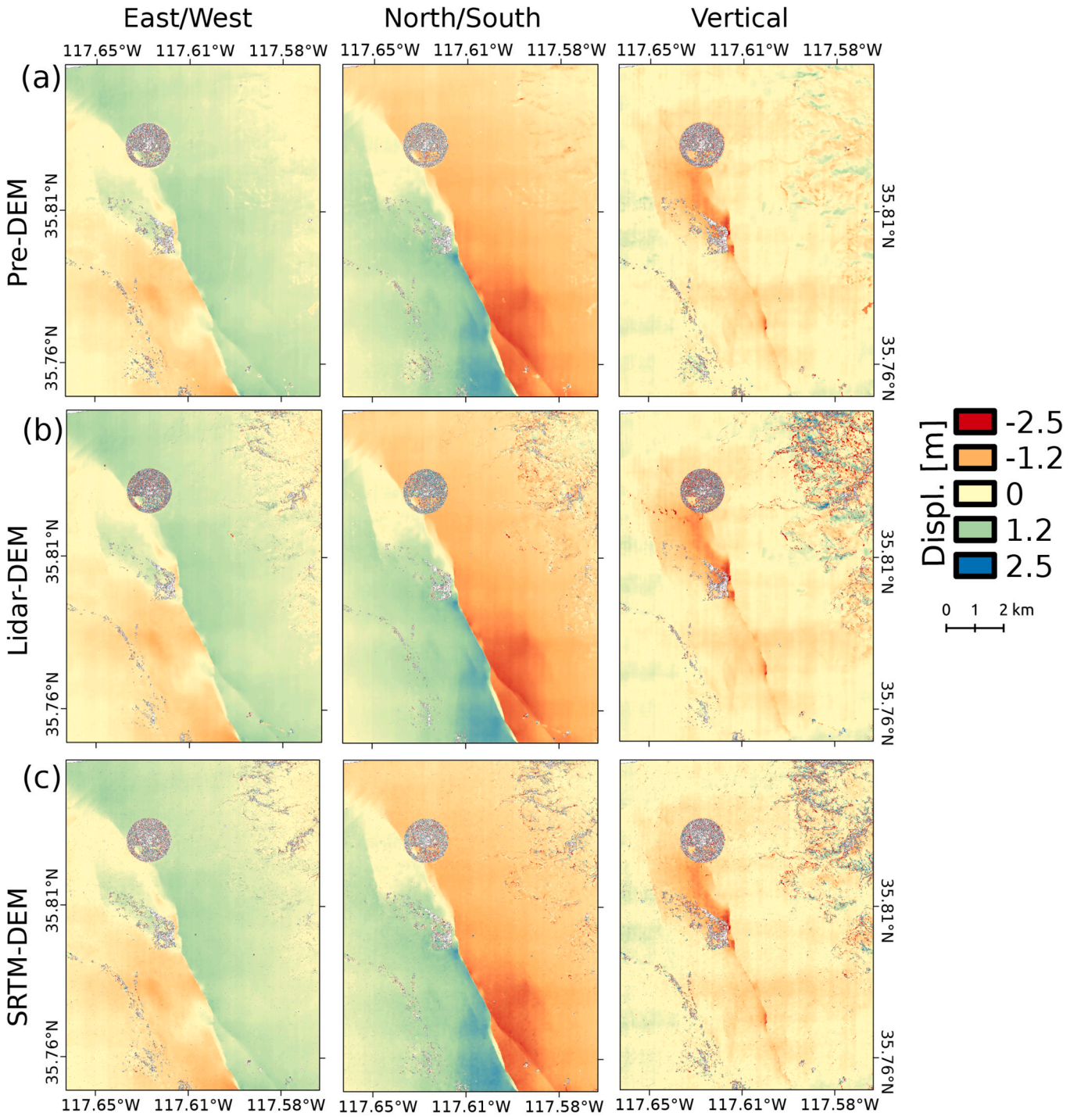

Fig. 9. 3D-displacement maps using our approach. The method was applied to the same data set as in Fig. 8. The first and second columns correspond to the horizontal displacement. The third column corresponds to the vertical displacement. The method was tested using three reference DEMs: Pre-DEM (1 m), LidarDEM (10 m), and SRTM DEM (30 m).

described in Section 3.1. Points with poor correlation were filtered out based on correlation criteria. Afterward, selected tie points were transformed to a projected coordinate system (UTM 11 N) using the geotransform respective to each ortho-image (k). Subsequently, horizontal errors at all virtual control points (vCP) were computed for each orthoimage: $\Delta X_i^k = (X_{vCPi}^{ref} - X_{vCPi}^{orthok})$ and $\Delta Y_i^k = (Y_{vCPi}^{ref} - Y_{vCPi}^{orthok})$. Ultimately, the horizontal errors (ΔX_i^k, ΔY_i^k) were used to compute the registration uncertainty and statistics to assess the performance (e.g., the circular errors at the 68% 68CE ($\sim 1\sigma$) and 90% 90CE ($\sim 1.4\sigma$) confidence level).

It should be emphasized that we selected different GCPs from the ones used for the RSM-refinement to assess the ortho-images geolocation accuracy.

Fig. 4-a shows an example of measured error in one ortho-image orthorectified using three different DEMs. The 68CE and 90CE values are reported in the plots of Fig. 4-b-c and summarized in Table 2.

Our RSM refinement approach consistently yields a more accurate geolocation of the ortho-images than the specification given by Digital Globe and Airbus, which report a 90CE $\sim$ 3-5 m for ortho-images acquired at off-nadir angles $<15°$. Moreover, one can observe from values

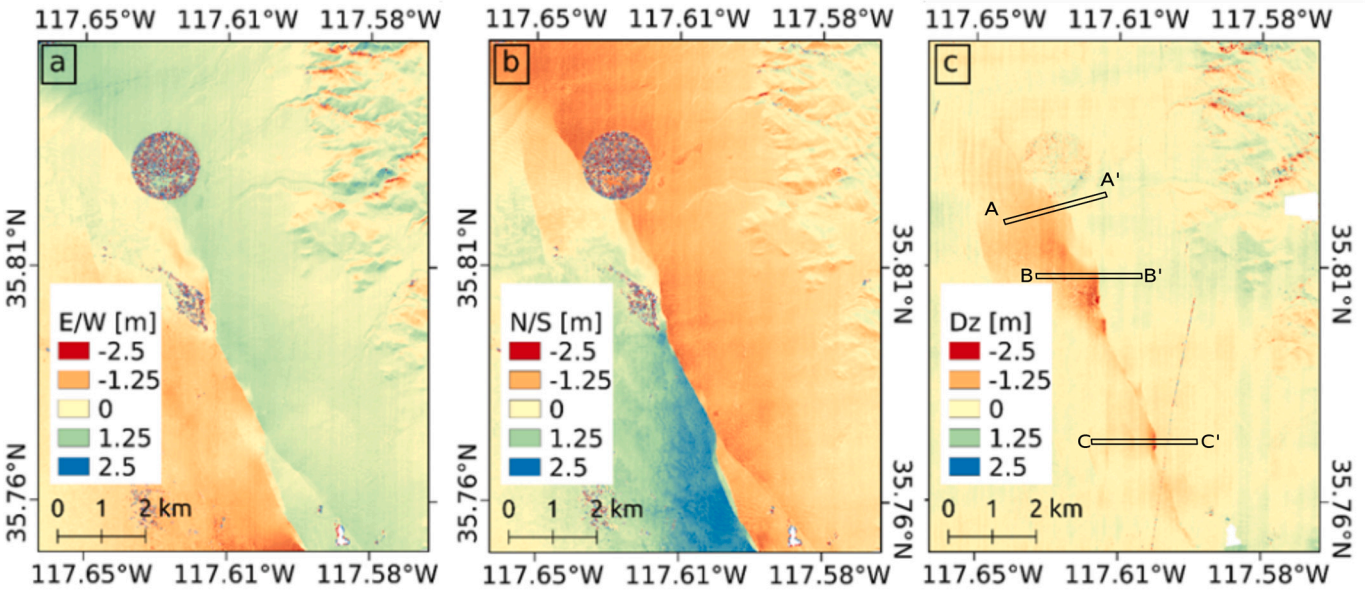

Fig. 10. Overview of produced 3D displacement using the state of the art method. (a, b) 2.4-m resolution horizontal surface displacement field of the M_w 7.1 Ridgecrest. (a) East/West component and (b) North/South component. The horizontal displacement was derived by correlating two images bracketing the earthquake using a multi-scale subpixel frequency correlator. (c) Vertical displacements are derived by differencing pre-and post- DEM.

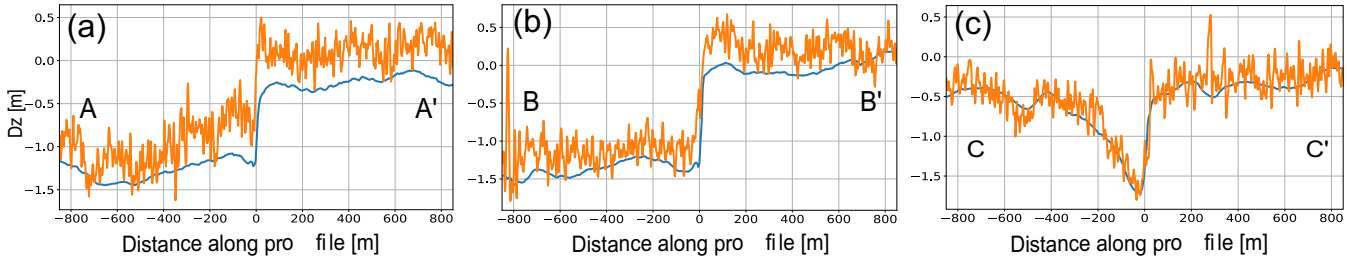

Fig. 11. Comparison of vertical displacements measured from our approach and sate-of-the-art method. Blue profiles corresponded to the measurement using our method, and orange profiles to the measurement from the stat-of-the-art method. Profiles extracted along (a) AA', (b) BB' and (c) CC', respectively. See Fig. 10-c for profiles locations. (For interpretation of the references to colour in this figure legend, the reader is referred to the web version of this article.)

summarized in Table 2 and Table S.2 that the horizontal accuracy depends on the ground sampling distance (GSD) of produced images, the quality of the *rDEMs* and the image acquisition parameters (mainly off-nadir angles).We note that the geolocation accuracy also depends on:

(1) The geolocation accuracy of the reference image (NAIPs) which is reported to be ~5 m at 95CE (Earth Resources Observation and Science (EROS) Center, 2017). Therefore, by design, our procedure cannot yield a more accurate geolocation.
(2) The environmental surface changes between the 3D-set ortho-images and the ref-image, that is a function of the difference in acquisition date, sensors characteristics and acquisition condition. The accuracy of the geolocation is degraded where such changes are most significant.
(3) The number of *vCPs* and their distribution within the scene. They should be selected on flat areas to avoid both parallax effects and shadows, and cover the entire extent of the scene for highest accuracy.

However, for the *vCPs* selected for the geolocation assessment, we did not consider all these criterions. Therefore, much of the observed residual spread can be attributed to change in landscape and terrain characteristics (i.e., earthquake surface deformation) over time, which on the one hand, leads to errors in extracted *vCPs* for the geolocation analysis of generated ortho-images. On the other hand, errors in the selected GCPs for the RSM-refinement result in an error in the linear coefficient of Eq.(2), and thus to a long-wavelength error in the displacement maps (Section 3.4). Overall, the circular errors range from 0.5 to >2 m, with a mean value of ~1.7 m. Similarly, residual errors in the horizontal geolocation accuracy ranges from 0.4 m to >3 m with a mean value of 1.92 m.

Table 2 and Fig. 4 also show that images orthorectified using the photogrammetric pre- and post-DEMs have slightly better horizontal geolocation accuracy than the images orthorectified using either the LiDAR or SRTM DEMs. The residual errors are the largest with SRTM, with a mean value of ~4 m ($RMSE_{xy}$) and a 68CE of ~3 m. The errors increase for larger off-nadir view angles. The 68 CE is on average 2.16 m for ortho-acquired at off-nadir angles >25° while it is ~1.74 m 68CE on average when all view angles are considered.

To quantify the impact of the correction term $\vec{\delta}(p)$ on the orthorectification process, we performed a correlation between pre- and post-images orthorectified using either the standard RPC-based method or our refinement method (Section 3.1). Fig. 5 shows the correlation results between the pre- and post-earthquake WV-2 images acquired on June 23, 2018, and July 14, 2019, respectively. The same parameters were selected for the correlation, and the same DEM, resampling kernel, and resolution for the orthorectification.

The test shows a horizontal bias of ~9 m in EW and ~ 18 m in NS

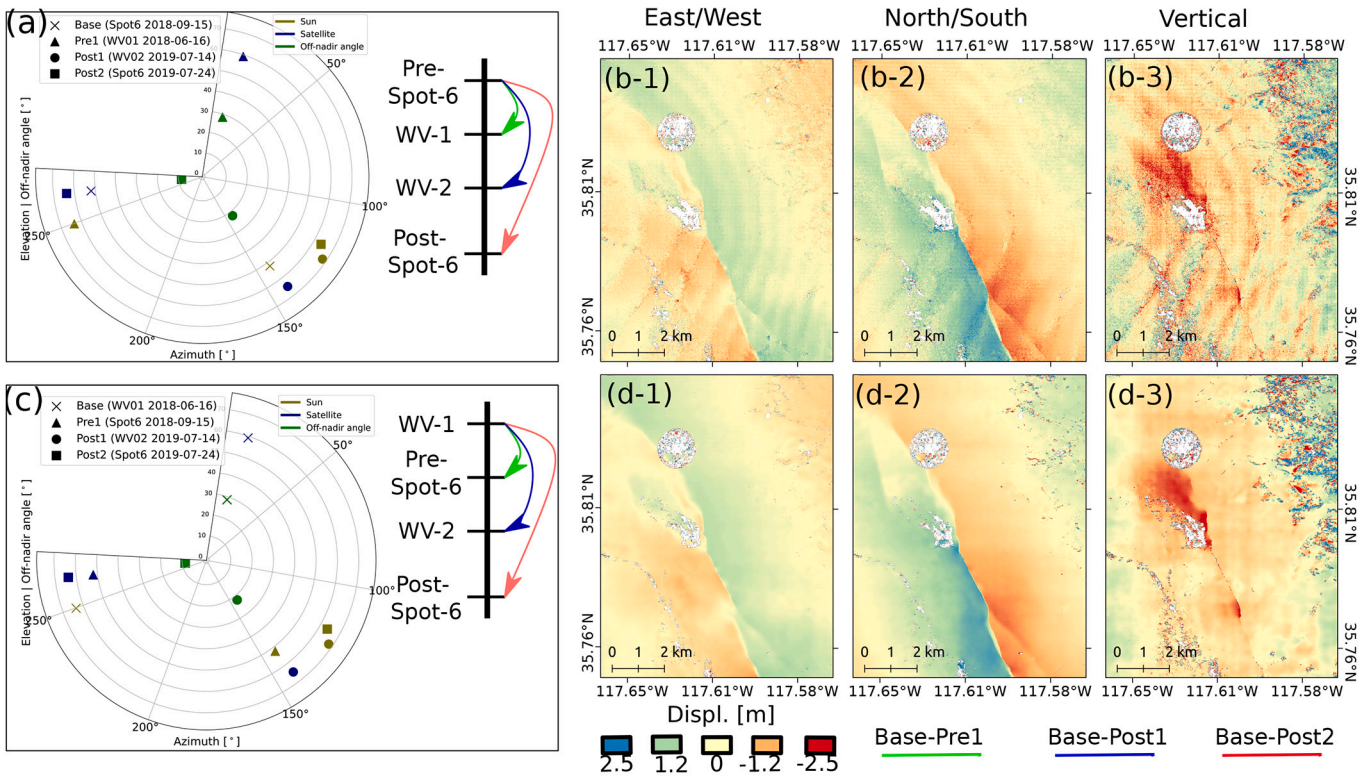

Fig. 12. Cross-platform 3D-displacement. (a,c) Sky plots of the 3D-set used for the displacement calculation, using Spot-6 and WV-1 as base image for correlation respectively. (b,d) Derived displacement measurements in EW (−1), NS (−2) and Dz (−3) directions, respectively.

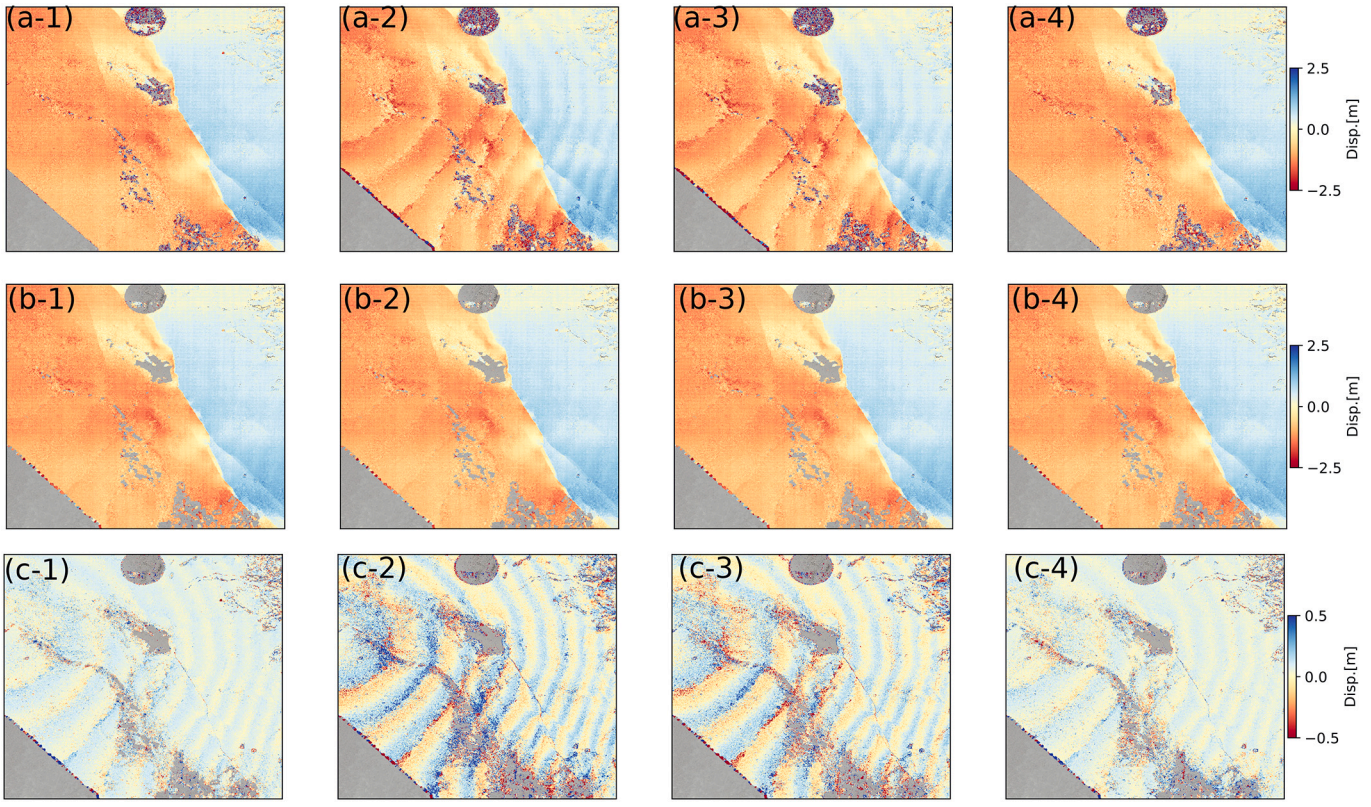

Fig. 13. East/West displacement component of the cross-platform data cube. (a) The input E/W component of the data cube. (b) Reconstructed E/W component using the coseismic displacement source of the ICA decomposition corresponding to the coseismic displacement. (c) Displacement residuals reconstructed using the remaining sources of the ICA decomposition. (1–4) Correspond to the base image used for the correlation scheme (WV1, pre-Spot6, WV2, and post-Spot6, respectively).

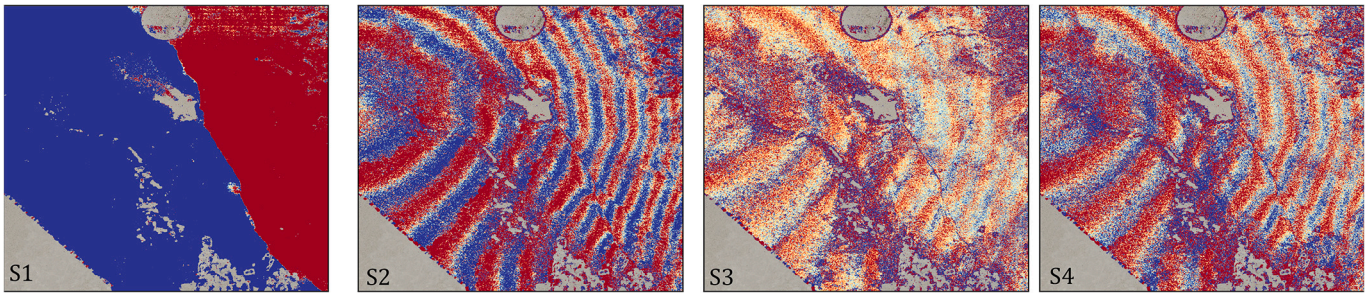

Fig. 14. A plot of independent sources extracted from the East/West cross-platform data cube.

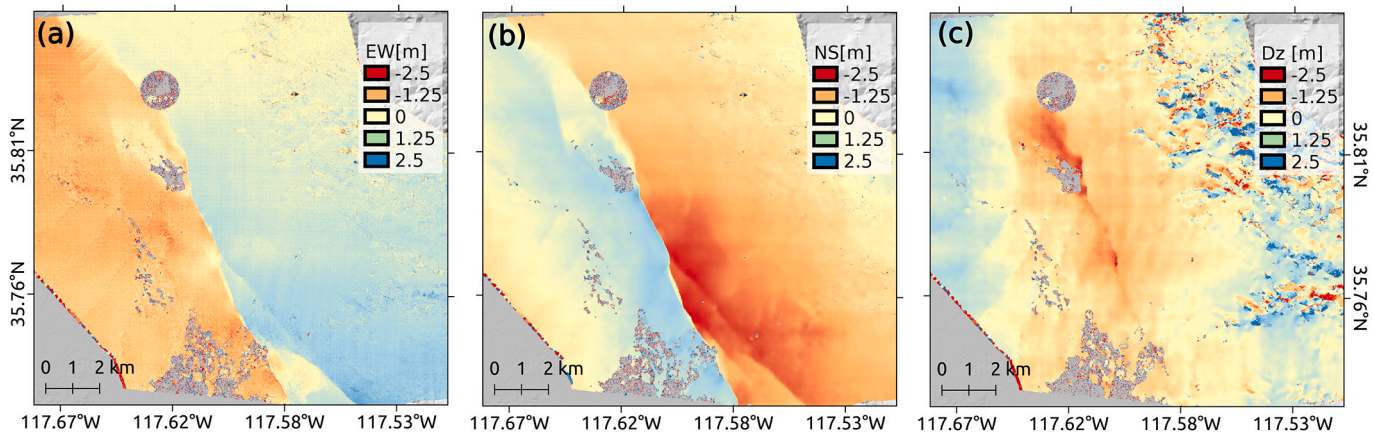

Fig. 15. Overview of the 3D-displacement measurements produced using the average stack of the extracted component corresponding to the coseismic displacement.

when the images orthorectified with the standard method are used. In addition, we observe a large magnitude parallax related to the topography that was not resolved correctly during the orthorectification process, mainly related to the attitude variation during image acquisition. By contrast, our refinement method reduces the average horizontal geolocation accuracy in the EW and NS to ~0.5 m and the parallax due to topography.

The impact of the correction is best observed when we correlate the same single image (e.g., WV2 image acquired on July 14, 2019), where the base image is orthorectified with the standard method and the target image orthorectified with our method (Fig. 6). Thus, the correction matrix A is mainly a global correction of the satellite look direction that compensates for any drift along the satellite trajectory and attitude (roll, pitch, and roll).

5.1.2. *Artifacts*

To identify the different sources of errors and the bias that could affect the displacement measurements, we orthorectified a *3D-set* composed of four Digital Globe images (WV3 acquired on September 8, 2016, WV1 acquired on June 18, 2018, WV2 acquired on July 14, 2019 and WV1 acquired on June 21, 2020) at 60-cm ground sampling distance using the high-resolution DEMs (1-m GSD) produced from photogrammetry using data either before or after the event. Then, three horizontal surface displacement fields with 2.6-m GSD were derived by correlating the base image (WV3) to the three target images (pre1-WV1, post1-WV2 and post2-WV1). The acquisition parameters of the images in this *3D-set* and the correlation results are shown in Fig. 7. The measurements show strong linear stripe artifacts caused by misalignment of the CCD arrays, a common problem in push-broom imaging systems that generally use a sensor formed of staggered line arrays of CCD. The misalignments are generally small (typically less than 1/10 of the pixel size) within a single array and larger (possibly up to 1/2 of the pixel size) at the junctions between different arrays. The observed spaced stripes in Fig. 7-a in the North/South component of the computed horizontal displacement map are correlated with the corresponding spatial positions of the CCD sensors in the base and target images. Consequently, the measured horizontal displacement is biased by ~40 cm (~0.7 pix). The amplitude of the geometric distortion caused by the CCD misalignment is estimated from the disparity map computed between two pre-event images where there is no coseismic deformation (Fig. 7-a). This map also shows a linear striping artifact typical of jitter running in the satellites' along-track direction with an amplitude of ~40 cm and topographic artifacts due to DEM inaccuracies.

Furthermore, another type of artifact typical of aliasing was identified when correlating two SPOT-6 images bracketing the earthquake, as reported by Milliner et al. (2021). Two Spot images, with a similar geometry acquisition and a low view angle (<10°), were orthorectified to 1.5 m GSD using the same pre-event photogrammetric DEM and then correlated using a multi-scale (128 × 128 to 32 × 32 pixels) sub-pixel phase correlator with an 8-pixel step, resulting in a 12 m GSD displacement map. As shown in Fig. 7-c, the fault rupture is identifiable, and no topography-dependent artifacts are observed; however, the measurements are biased with an aliasing artifact (amplitudes are up to ~50 cm) caused by the two images. We suspect that this artifact arises due to the resampling procedure used by the provider to generate the super-resolution images.

The different components of the error source that bias the displacement field must be taken into account and eventually corrected for, in order to produce high-quality measurements of the displacement field (i.e., with the highest possible spatial resolution, and reduced artifacts).

Our measurements show that the main sources of errors include: (1) the unmodelled interior orientation (i.e., stripe artifacts), (2) the satellite attitude variation (i.e., time-varying attitude jitter), (3) resampling errors in the generation of the images distributed by the providers (i.e., aliasing artifacts), (4) the image acquisition geometry and DEM quality used for the orthorectification (i.e., topography-dependent artifacts),

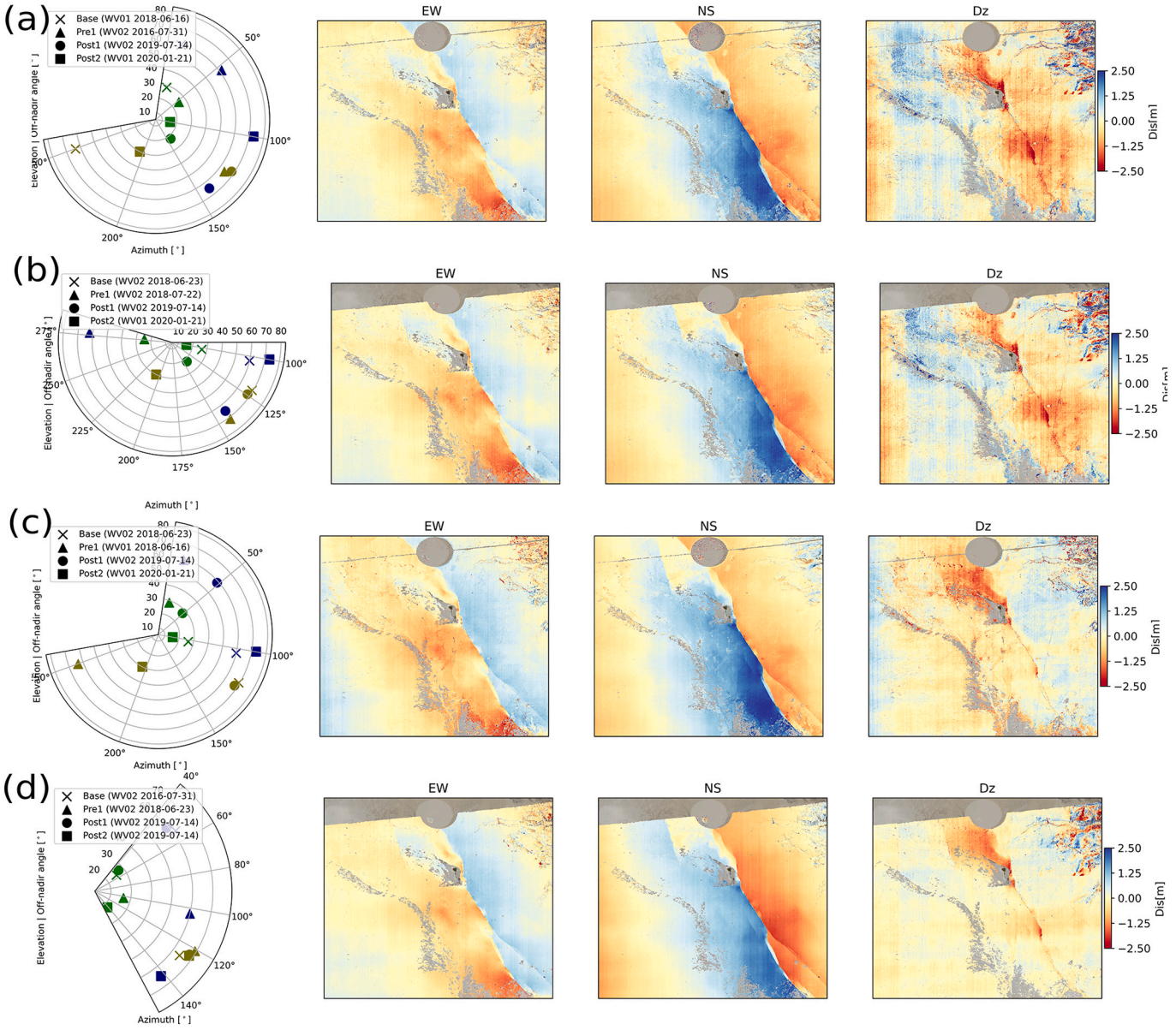

Fig. 16. Example of 3D-displacement maps computed with 4 different combinations of images.

and (5) texture and radiometry changes between the base and the target images (i.e., decorrelation noise).

5.2. State-of-the-art 2-D measurements of horizontal displacements

We first measured horizontal displacements using the state-of-the-art method based on the correlation of orthoimages. Four input images are selected: WV-1 and WV-2 before the earthquakes and in-track stereo pairs of WV-2 after the earthquakes (see sky plot in Fig. 8-d). Each of these images is orthorectified to 60 cm GSD using three different pre-event DEMs. We use only a single DEM because, most often, it is not possible to construct or have access to both a pre- and a post-event DEM. The three DEMs considered in this case are the SRTM (30 m), LiDAR DEM (10 m), and photogrammetric DEM extracted using WV-2 stereo pairs acquired on July 14, 2019 (with 2 m GSD). The orthoimages are then correlated using a 32 × 32 pixel window with an 8-pixel sliding step, yielding in 4.8 m resolution displacement maps. Before performing the orthorectification, "wv_correct" an ASP routine, is used to regenerate images corrected for CCD artifacts; this routine is specific only for WV-1 and WV-2 imagery.

The North/South components of the horizontal displacement are presented in Fig. 8-a,b and -c. The base-pre1 correlation, which is the correlation between two pre-event images, should in principle show no displacements, and reveal only noise measurements. Topographic artifacts are clearly present though. In the base-post1 and base-post2 measurements, a discontinuity that represents the surface rupture caused by the M_w 7.1 earthquake is identifiable. In absence of any bias, the two displacement measurements should lead to the same result, which is not the case here. We can therefore see that the horizontal measurements depend on the acquisition geometry as well as the rDEM used for the orthorectification. In addition, less decorrelation and topographic artifacts are observed when a photogrammetric DEM extracted from the input images is used for the orthorectification. The measurement of the displacement also shows that the linear artifacts CCD are reduced compared to Fig. 7-b but not completely removed; residual CCD misalignments are still observed.

The horizontal results and identified artifacts derived from the abovementioned approach are consistent with horizontal measurements

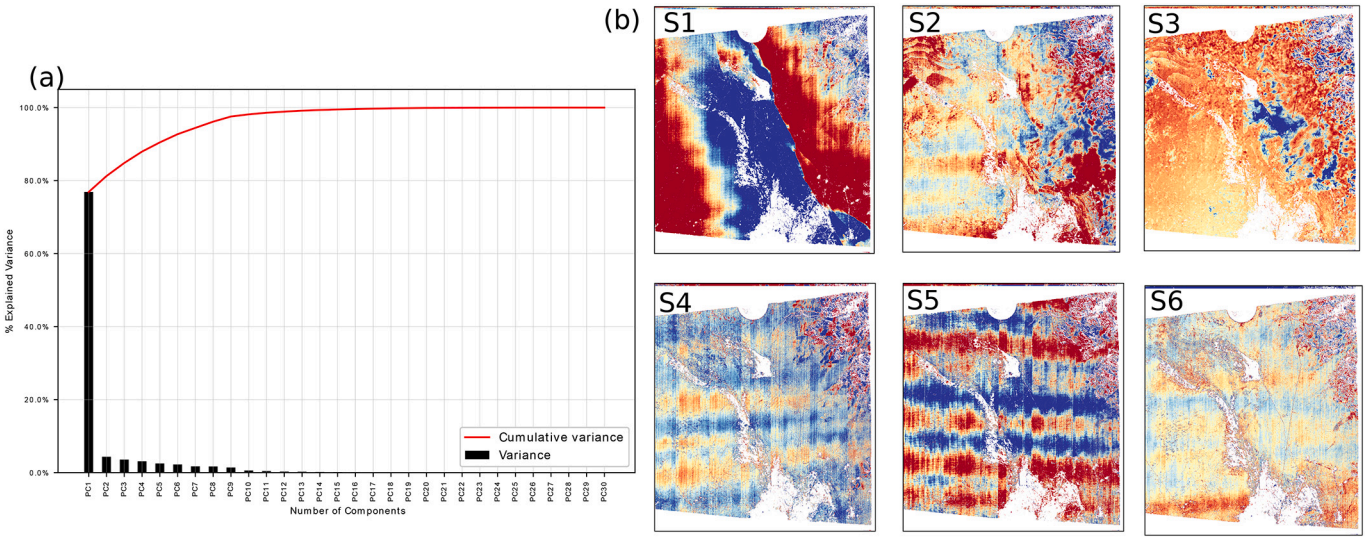

Fig. 17. Example of sources extracted from the East/West data cube. (a) Histogram and cumulative variance distribution of extracted sources. (b) Example of the spatial distribution of the primary sources.

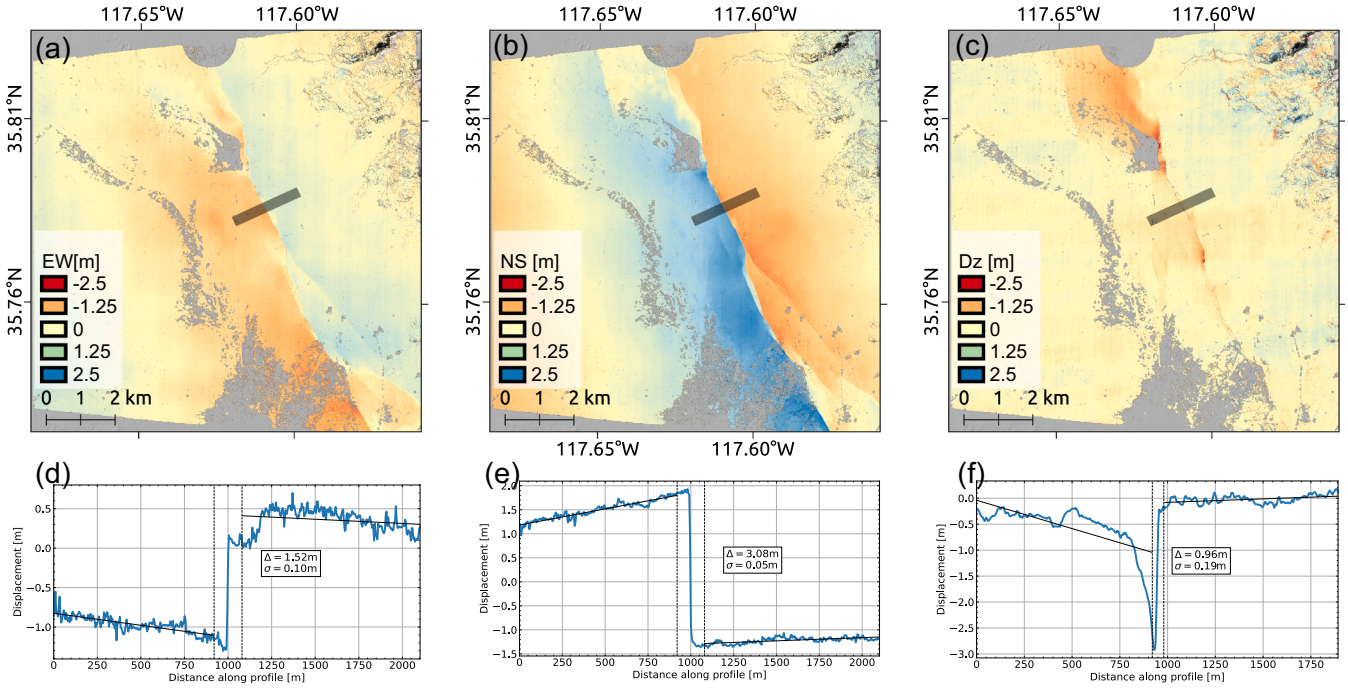

Fig. 18. Reference 3D-displacement measurements. (a-c) Colour maps represent the East/West, North/South, and vertical ground displacement, respectively. (d-f) profiles extracted along the respective black box in panels (a-c).

from other studies based on similar methods applied to lower-resolution sensors, including Sentinel-2 and PlanetScope (Milliner & Donnellan, 2020), and higher-resolution sensors, including SPOT-6 (Milliner et al., 2021), WorldView (Barnhart et al., 2020), and Pléiades (Antoine et al., 2021).

5.3. 3D-displacements measured from our workflow

We ran the workflow described in section 3 using the same *3D-set* presented in the previous section (see sky plot in Fig. 8-d). Fig. 9 shows the computed 3D-displacement measured using the single correlation strategy option with WV-1 acquired on June 16, 2018, selected as the base image.

Analysis of the horizontal components (~ 2.4 m GSD) reveals a substantial improvement of the measurement that is no longer sensitive to the rDEM used for the orthorectification. The insensitivity to the rDEM characteristics is also demonstrated by comparing profiles (Fig. S.1 and Table S.3). Furthermore, because we triangulate the correlation measurements at each sampling point, the topographic residuals (i.e., the unresolved parallax during the orthorectification process) are reduced, and the vertical component is extracted with proper account for topographic changes. It should be noted that, with our method, the measured vertical displacement is not affected by the horizontal advection caused by the coseismic deformation, which can be the case using the state-of-the-art method. We also observe some artifacts typical of jitter, which are more prominent in the vertical

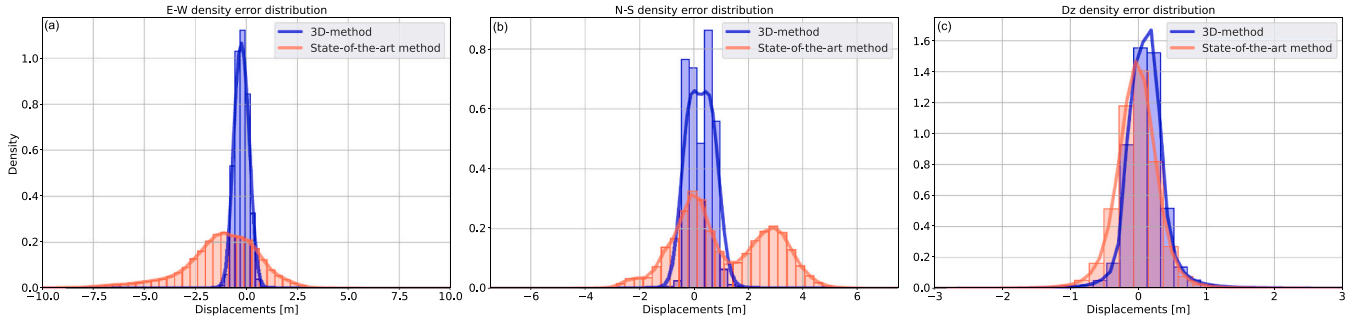

Fig. 19. Error distribution example. Histograms of the relative offsets between the reference 3D-displacement and the state-of-the-art method (orange histograms) and between the reference 3D-displacement and the 3D-correlation approach with only 4-images (blue histograms). (a) EW histograms of the density error distribution. (b) NS histograms of the density error distribution. (c) Dz histograms of the density error distribution. (For interpretation of the references to colour in this figure legend, the reader is referred to the web version of this article.)

component.

The average vertical displacement is between 1.5 m and − 1.5 m. Looking at area far from the rupture, where vertical displacements are small <0.8 m based on InSAR and GNSS measurements (Jin and Fialko, 2020; Ross et al., 2019), we measure ~0.5 m, which gives a first-order estimate of the uncertainty.

The results obtained from applying our workflow confirm that high-quality 2D/3D displacement measurements can be produced using a publicly available coarse resolution rDEM, typically with SRTM. Therefore, our approach is not limited by the availability of an updated high-resolution DEM and compared to a purely 2-D workflow, improves the quality of the measurements of the horizontal displacement field.

5.3.1. *Comparison of displacements measured from 3-D correlation and state-of-the-art method*

The 3D surface displacement field due to the Ridgecrest earthquake sequence was measured in previous studies by combining the standard 2-D workflow procedure with DEM differencing informally known as the "2.5 D method", as outlined in section 2 (Antoine et al., 2021; Barnhart et al., 2020). In order to compare our approach to this more standard method, we have reproduced the displacement results presented in Barnhart et al. (2020) using two sets of Digital Globe stereo-pairs acquisitions. The first stereo-pair of WV-1 acquired on June 16, 2018, before the Ridgecrest earthquakes, and the second stereo-pair of WV-2 acquired after the earthquakes on July 14, 2019 (Table S1). The two sets of stereo-data were processed separately to produce pre-and post-DSM at 2-m GSD using the OrthoEngine module of PCI Geomatics software (details on DEM extraction are provided in the supporting information). Then, the misregistration between the two DEMs was reduced by extracting a sub-region located far from the surface ruptures. The horizontal surface displacement was retrieved using sub-pixel image correlation in the frequency domain between pre-and post- orthorectified images. For each date, the image with the smallest off-nadir angle (28.6° and 27.6°) is orthorectified with the high-resolution pre- and post- DEM, respectively, with the purpose of limiting as much as possible the stereoscopic effects. The NS and EW horizontal displacements with 2.4-m GSD are shown in (Fig. *10*-a,b). Ames Stereo Pipeline software is used to correct for Digital Globe images CCD misalignment, while the orthorectification and correlation processes are performed using COSI-Corr^{+}. The vertical displacement is computed by simply differencing the two DEMs without accounting for the horizontal displacement. As stated by Barnhart (2020, 2019), if the topography is relatively flat, as is the case for most of the valley where the Ridgecrest earthquakes occurred, the horizontal displacement of the topography should not bias the vertical component on average. It is, however, a source of noise due to the roughness of the topography.

The correlation of the pre-and-post shaded DEMs (Fig.S 2) actually shows some measurable deformation signal despite the lower resolution of the DEMs compared to the images. The state-of-the-art approach yields in a biased displacement arising due to lateral shift of the topography during the earthquake. The bias is between 1.6 m and 2 m on average (Fig. S2f-g). In general, the topography differencing will reflect the combined effects of misregistration, resampling errors, and unaccounted advective transport of the topography. By contrast, our method solves for the 3D displacement in all 3 directions independently and it is insensitive to the choice of the rDEM. Fig. *11* shows an example of profiles extracted from the vertical component measured by our method and by the state-of-the-art method.

5.4. *Cross-platform 3D-displacement*

In this section, the 3D-displacement field was retrieved using a *3D-set* composed of images from different platforms; we combined WV1, WV2, and Spot-6 (see sky plots in Fig. *12*) for more information on geometry and acquisition dates). The 3D-set images were orthorectified using the LiDAR DEM to a 1.5 m resolution, which corresponds to the spatial resolution of the panchromatic band of Spot-6 imagery. Initially, we adopted a single correlation scheme by selecting the pre-event Spot-6 image as the base image. Analysis of the resulting 3D-displacement reveals a pattern of aliasing that bias the measure in all directions (Fig. *12*-b) as noted above and reported by Milliner et al. (2021).

A first approach to mitigate this artifact is to change the base image to avoid cross-correlation between the pre- and post- Spot-6 ortho images. Fig. *12*-d shows the produced displacement measurements with WV-1 selected as the base-image. An improvement in the measurements can be noticed, there is no longer interference between the resampling artifact from the pre- and post- images, and the aliasing pattern disappears; however, the original resampling artifacts are still present and are not corrected. This approach would be effective when the coseismic displacement amplitude is larger than the amplitude of the resampling errors, which we estimate to be about ~1/10 pixel (~15 cm). Therefore, within this approach, we actually do not remove the artifact. Instead, we show later a post-processing scheme to correct it.

To give equal weight to all the images, we constructed a data cube of 4 displacement maps by varying the base image (see section 3.5). Each displacement map in this data cube should contain the same deformation signal with additional artifacts of varying amplitude and nature depending on the choice of the base image. As it can be seen in the East/West component of the data cube (Fig. *13*-a), there are two displacement maps where the aliasing pattern is clearly identifiable. They correspond to the scheme in which we have chosen one of the two SPOT images as a base-image.

By applying the geoICA decomposition to the data cube, we separated the coseismic displacement from artifacts sources that correspond mainly to the aliasing artifact. The extracted sources for the East/West component are presented in Fig. *14*. As expected, the deformation signal,

easily identifiable from the discontinuity due to the surface ruptures, shows up in only one component (S1). Therefore, the 3D-displacement map was produced using only this source. Fig. *13*-b reports the extracted deformation signal, and Fig. *13*-c represents the artifact. The final displacement maps were generated by stacking the 4 displacement maps reconstructed from only the S1 component. As a result, we observe a considerable improvement in the 3D displacement map, and the various artifacts due to the Jitter, CCD misalignments, or resampling errors are not visible anymore (Fig. *15*).

5.5. Generation of a reference 3D-displacement

The ICA decomposition can be applied to any data cube when provided at least two images before and two images after the deformation event. In principle, including more data should help remove the noise further. In this section, we use a 3D-set consisting of 7 images (3 acquired before the earthquakes and 4 acquired after) over the region of interest 1 (ROI 1). Table S.3 provides detailed information about the selected 3D-set images.

The input 3D-set images were orthorectified with the LiDAR DEM at 60 cm GSD. Then, by applying the progressive correlation strategy, 42 correlation maps were generated, yielding in 72 3D-displacement maps ($A_3^2C_4^2 + C_3^2A_4^2$, where A and C stand for arrangement and combination, respectively). The WV1 and WV2 images were corrected for CCD artifacts using ASP utility "wv_correct" before the orthorectification process. The resulting data cubes were composed of 72 observations in each direction, and pixel measurements with a displacement of more than 20 m were considered outliers and discarded.

An example of the computed displacement maps is shown in Fig. *16* (an animation with all the results is available in the supplementary materials).

Visual assessment reveals that the vertical components vary depending on the acquisition geometry of the satellites, while the horizontal components are more stable. In addition, linear stripes are observed along and across the displacement maps, which are typical of CCD misalignment and jitter, respectively. Residual CCD misalignments are still even after applying a CCD correction procedure (Shean et al., 2016) on WV1 and WV2 and refining the physical model.

Then, to take advantage of the observation redundancy, the ICA decomposition was performed on the data cubes to extract a reference displacement signal free of residual artifacts. By looking at the variance of the various source components, we see that one component accounts for most of the data variance (Fig. *17*-a), and seven other significant components that represent the artifacts. The data variance explained by the different source components in the case of the E/W data cube is shown in Fig. *17*-a. Fig. *17*-b also represents a spatial visualization of the extracted dominant components. The dominant component (S1) clearly represents the coseismic signal. Again, the other source components show linear stripes along- and across-track, typical of CCD misalignment and jitter artifacts, which are clearly highlighted in panels S4 and S5 from Fig. *17*.

The sources also account for persistent topographic artifacts (Fig. *17*-b(S3)) that were not resolved during the orthorectification and *3D-Computing* steps (see sections 3.2 and 3.4). We use the only source component (S1) corresponding to the coseismic signal (Fig. *17*-b(S1)) to reconstruct the data cube, which amounts to saying that we are filtering out the sources of artifacts represented by the other components. We then stack all the EW, NS, and vertical maps to produce a 3D-displacement map that we consider free from artifacts and the most accurate signal extracted from all the data assembled for this study. We recommend using this reference measurement in further investigations of the Ridgecrest earthquake sequence. Fig. *18* represents the produced reference displacement measurements.

6. Error quantification

We now use the reference 3-D displacement map described in the preceding section to evaluate the errors contained in the measurement made from a minimum 3D-Set of 4 images and measurement generated from the state-of-the-art method. Histograms in each dimension are given in Fig. *19*. The spread of our 3D method is Gaussian and can be seen as reflecting the noise of the measurements. Therefore, on average, the uncertainty on the NS, EW, and vertical displacement measurements is ~0.6 m, ~0.7 m, and ~ 0.6 m at the 90% confidence level, respectively. However, with the state-of-the-art method, the standard deviation of the Gaussian distribution, on average, of the EW component is ~2.18 m and of the NS component, ~2.5 m, while for the vertical component is ~0.7 m. Artifacts related to topography, jitter, and CCD misalignment are forming the tails of the state-of-the-art method histogram.

7. Conclusions

We present in this study a new approach to measure ground deformation in 3D from optical satellite images, which is applicable if at least 2 pairs of images are available before and after a deformation event. The addition of an ICA-based post-processing allows to take advantage of data redundancy to separate the deformation signal from the various sources of artifacts that are typical of satellite imaging systems related to the internal (CCDs misalignment in particular), the external models (the telescope position and viewing direction during the image acquisition) and the production of the images distributed by the providers (resampling bias). In any case, the method yields the 2-D displacement field with significantly better accuracy than a standard correlation of orthoimages, even if the orthorectification procedure is optimized to correct misregistration arising from errors on the internal and external models. Vertical displacements can be resolved if the viewing angles span a sufficiently large range of values ($> 8°$) to allow for the measurable stereoscopic offsets. The procedure makes use of a reference DEM, but the outcome is independent of the characteristics of the chosen DEM, which is not the case with the standard approach. We used the case-example of the ground deformation caused by the Ridgecrest earthquake sequence to assess the performance of our proposed approach. We were able to generate high-quality measurements of coseismic ground displacement with GSD of 2.4 m, and uncertainties at the 90% confidence level on the NS, EW, and vertical displacement measurements of 0.6 m, 0.7 m, and 0.6 m, respectively. The technique could similarly be used to study other processes causing displacements of the earth surface, such as slow landslide, sand dune migration, volcanic deformation, and ice flow.

Author contribution

SA: Method design, data processing, manuscript preparation (text and figures); JPA: Supervision, manuscript preparation, funding. All authors edited the manuscript and agreed to the published version of the manuscript.

Author statement

Saif Aati Method design, data processing, manuscript preparation (text and figures); **Jean-Philippe Avouac**: Supervision, manuscript preparation, funding. All authors edited the manuscript and agreed to the published version of the manuscript.

Declaration of Competing Interest

None

Acknowledgments

The authors would like to thank Marc-Pierrot Deseilligny and Ewelina Rupnik for helpful discussions. The authors are very grateful to the editor, associate editor, and reviewers for their comments and suggestions, which helped improve the paper.

We acknowledge the ©2020 Digital Globe/NextView licensing agreement, through which we accessed the WorldView imagery used in this study.

Appendix B. Supplementary data

Supplementary data to this article can be found online at (Aati, 2021) https://zenodo.org/record/5831941.

References

Aati, S., 2021. A New Method for 2-D and 3-D Precise Measurements of Ground Deformation from Optimized Registration and Correlation of Optical Images and ICA-Based Filtering of Image Geometry Artifacts. https://doi.org/10.5281/zenodo.5831941.

Aati, S., Avouac, J.-P., 2020. Optimization of optical image geometric modeling. Application to Topography Extraction and Topographic Change Measurements Using PlanetScope and SkySat Imagery 25. https://doi.org/10.3390/rs12203418.

Altena, B., Kääb, A., 2017. Elevation change and improved velocity retrieval using orthorectified optical satellite data from different orbits. Remote Sens. 9, 300. https://doi.org/10.3390/rs9030300.

Antoine, S.L., Klinger, Y., Delorme, A., Wang, K., Bürgmann, R., Gold, R.D., 2021. Diffuse Deformation and Surface Faulting Distribution from Submetric Image Correlation along the 2019 Ridgecrest, California, Ruptures, p. 28.

Avouac, J.-P., Leprince, S., 2015. Geodetic imaging using optical systems. In: Treatise on Geophysics. Elsevier, pp. 387–424. https://doi.org/10.1016/B978-0-444-53802-4.00067-1.

Ayoub, F., Leprince, S., Binet, R., Lewis, K.W., Aharonson, O., Avouac, J.-P., 2008. Influence of camera distortions on satellite image registration and change detection applications. In: IGARSS 2008–2008 IEEE International Geoscience and Remote Sensing Symposium. Presented at the IGARSS 2008–2008 IEEE International Geoscience and Remote Sensing Symposium. IEEE, Boston, MA, USA. https://doi.org/10.1109/IGARSS.2008.4779184 p. II-1072-II–1075.

Ayoub, F., Leprince, S., Avouac, J.-P., 2009. Co-registration and correlation of aerial photographs for ground deformation measurements. ISPRS J. Photogramm. Remote Sens. 64, 551–560. https://doi.org/10.1016/j.isprsjprs.2009.03.005.

Barišin, I., Hinojosa-Corona, A., Parsons, B., 2015. Co-seismic vertical displacements from a single post-seismic lidar DEM: example from the 2010 El Mayor-Cucapah earthquake. Geophys. J. Int. 202, 328–346. https://doi.org/10.1093/gji/ggv139.

Barnhart, W.D., Gold, R.D., Hollingsworth, J., 2020. Localized fault-zone dilatancy and surface inelasticity of the 2019 Ridgecrest earthquakes. Nat. Geosci. 13, 699–704. https://doi.org/10.1038/s41561-020-0628-8.

Besl, P.J., McKay, N.D., 1992. A method for registration of 3-D shapes. IEEE Trans. Pattern Anal. Mach. Intell. 14, 239–256. https://doi.org/10.1109/34.121791.

Beyer, R.A., Alexandrov, O., McMichael, S., 2018. The Ames stereo pipeline: NASA's open source software for deriving and processing terrain data. Earth Space Sci. 5, 537–548. https://doi.org/10.1029/2018EA000409.

Bontemps, N., Lacroix, P., Doin, M.-P., 2018. Inversion of deformation fields time-series from optical images, and application to the long term kinematics of slow-moving landslides in Peru. Remote Sens. Environ. 210, 144–158. https://doi.org/10.1016/j.rse.2018.02.023.

Chen, K., Avouac, J.-P., Aati, S., Milliner, C., Zheng, F., Shi, C., 2020. Cascading and pulse-like ruptures during the 2019 Ridgecrest earthquakes in the Eastern California Shear Zone. Nat. Commun. 11, 22. https://doi.org/10.1038/s41467-019-13750-w.

Dalla Mura, M., Villa, A., Benediktsson, J.A., Chanussot, J., Bruzzone, L., 2011. Classification of hyperspectral images by using extended morphological attribute profiles and independent component analysis. IEEE Geosci. Remote Sens. Lett. 8, 542–546. https://doi.org/10.1109/LGRS.2010.2091253.

Earth Resources Observation aAnd Science (EROS) Center, 2017. National Agriculture Imagery Program (NAIP). https://doi.org/10.5066/F7QN651G.

Farr, T.G., Rosen, P.A., Caro, E., Crippen, R., Duren, R., Hensley, S., Kobrick, M., Paller, M., Rodriguez, E., Roth, L., Seal, D., Shaffer, S., Shimada, J., Umland, J., Werner, M., Oskin, M., Burbank, D., Alsdorf, D., 2007. The shuttle radar topography mission. Rev. Geophys. 45 https://doi.org/10.1029/2005RG000183.

Forootan, E., Awange, J.L., Kusche, J., Heck, B., Eicker, A., 2012. Independent patterns of water mass anomalies over Australia from satellite data and models. Remote Sens. Environ. 124, 427–443. https://doi.org/10.1016/j.rse.2012.05.023.

Gualandi, A., Serpelloni, E., Belardinelli, M.E., 2016. Blind source separation problem in GPS time series. J. Geod. 90, 323–341. https://doi.org/10.1007/s00190-015-0875-4.

Holland, P.W., Welsch, R.E., 1977. Robust regression using iteratively reweighted least-squares. Commun. Stat. - Theory Methods 6, 813–827. https://doi.org/10.1080/03610927708827533.

Hyvärinen, A., Oja, E., 2000. Independent component analysis: algorithms and applications. Neural Netw. 13, 411–430. https://doi.org/10.1016/S0893-6080(00)00026-5.

Jiang, Y., Cui, Z., Zhang, G., Wang, J., Xu, M., Zhao, Y., Xu, Y., 2018. CCD distortion calibration without accurate ground control data for pushbroom satellites. ISPRS J. Photogramm. Remote Sens. 142, 21–26. https://doi.org/10.1016/j.isprsjprs.2018.05.008.

Jin, Z., Fialko, Y., 2020. Finite slip models of the 2019 Ridgecrest earthquake sequence constrained by space geodetic data and aftershock locations. Bull. Seismol. Soc. Am. 110 https://doi.org/10.1785/0120200060.

Larochelle, S., Gualandi, A., Chanard, K., Avouac, J.-P., 2018. Identification and extraction of seasonal geodetic signals due to surface load variations. J. Geophys. Res. Solid Earth 123, 11031–11047. https://doi.org/10.1029/2018JB016607.

Leprince, S., 2008. Monitoring Earth Surface Dynamics with Optical Imagery (phd). California Institute of Technology. https://doi.org/10.7907/ZMTV-GV90.

Leprince, S., Barbot, S., Ayoub, F., Avouac, J., 2007. Automatic and precise orthorectification, coregistration, and subpixel correlation of satellite images, application to ground deformation measurements. IEEE Trans. Geosci. Remote Sens. 45, 1529–1558. https://doi.org/10.1109/TGRS.2006.888937.

Leprince, S., Muse, P., Avouac, J., 2008. In-flight CCD distortion calibration for pushbroom satellites based on subpixel correlation. IEEE Trans. Geosci. Remote Sens. 46, 2675–2683. https://doi.org/10.1109/TGRS.2008.918649.

Lowe, D.G., 2004. Distinctive image features from scale-invariant keypoints. Int. J. Comput. Vis. 60, 91–110.

Milliner, C., Donnellan, A., 2020. Using daily observations from planet labs satellite imagery to separate the surface deformation between the 4 July Mw 6.4 Foreshock and 5 July Mw 7.1 Mainshock during the 2019 ridgecrest earthquake sequence. Seismol. Res. Lett. 91, 1986–1997. https://doi.org/10.1785/0220190271.

Milliner, C., Donnellan, A., Aati, S., Avouac, J.-P., Zinke, R., Dolan, J.F., Wang, K., Bürgmann, R., 2021. Bookshelf kinematics and the effect of dilatation on fault zone inelastic deformation: examples from optical image correlation measurements of the 2019 Ridgecrest earthquake sequence. J. Geophys. Res. Solid Earth 126. https://doi.org/10.1029/2020JB020551 e2020JB020551.

Nissen, E., Maruyama, T., Ramon Arrowsmith, J., Elliott, J.R., Krishnan, A.K., Oskin, M. E., Saripalli, S., 2014. Coseismic fault zone deformation revealed with differential lidar: examples from Japanese Mw ~7 intraplate earthquakes. Earth Planet. Sci. Lett. 405, 244–256. https://doi.org/10.1016/j.epsl.2014.08.031.

Ross, Z.E., Idini, B., Jia, Z., Stephenson, O.L., Zhong, M., Wang, X., Zhan, Z., Simons, M., Fielding, E.J., Yun, S.-H., Hauksson, E., Moore, A.W., Liu, Z., Jung, J., 2019. Hierarchical interlocked orthogonal faulting in the 2019 Ridgecrest earthquake sequence. Science 366, 346–351. https://doi.org/10.1126/science.aaz0109.

Rupnik, E., Daakir, M., Pierrot Deseilligny, M., 2017. MicMac – a free, open-source solution for photogrammetry. Open Geospatial Data Softw. Stand. 2, 14. https://doi.org/10.1186/s40965-017-0027-2.

Shean, D.E., Alexandrov, O., Moratto, Z.M., Smith, B.E., Joughin, I.R., Porter, C., Morin, P., 2016. An automated, open-source pipeline for mass production of digital elevation models (DEMs) from very-high-resolution commercial stereo satellite imagery. ISPRS J. Photogramm. Remote Sens. 116, 101–117. https://doi.org/10.1016/j.isprsjprs.2016.03.012.

Shlens, J., 2014. A Tutorial on Independent Component Analysis. ArXiv14042986 Cs Stat.

Stumpf, A., Malet, J.-P., Delacourt, C., 2017. Correlation of satellite image time-series for the detection and monitoring of slow-moving landslides. Remote Sens. Environ. 189, 40–55. https://doi.org/10.1016/j.rse.2016.11.007.

Stumpf, A., Michéa, D., Malet, J.-P., 2018. Improved co-registration of Sentinel-2 and Landsat-8 imagery for earth surface motion measurements. Remote Sens. 10, 160. https://doi.org/10.3390/rs10020160.

Tang, Y., Li, L., Wang, C., Chen, M., Feng, W., Zou, X., Huang, K., 2019. Real-time detection of surface deformation and strain in recycled aggregate concrete-filled steel tubular columns via four-ocular vision. Robot. Comput.-Integr. Manuf. 59, 36–46. https://doi.org/10.1016/j.rcim.2019.03.001.

Tong, X., Xu, Y., Ye, Z., Liu, S., Tang, X., Li, L., Xie, H., Xie, J., 2015. Attitude oscillation detection of the ZY-3 satellite by using multispectral parallax images. IEEE Trans. Geosci. Remote Sens. 53, 3522–3534. https://doi.org/10.1109/TGRS.2014.2379435.

Ye, G., Pan, J., Zhu, Y., Jin, S., 2020. A jitter detection method based on the integration imaging model. ISPRS Ann. Photogramm. Remote Sens. Spat. Inf. Sci. V-3–2020, 709–715. https://doi.org/10.5194/isprs-annals-V-3-2020-709-2020.

Zhou, Y., Parsons, B., Elliott, J.R., Barisin, I., Walker, R.T., 2015. Assessing the ability of Pleiades stereo imagery to determine height changes in earthquakes: a case study for the El mayor-Cucapah epicentral area. J. Geophys. Res. Solid Earth 120, 8793–8808. https://doi.org/10.1002/2015JB012358.

Zinke, R., Hollingsworth, J., Dolan, J.F., Van Dissen, R., 2019. Three-dimensional surface deformation in the 2016 M $_W$ 7.8 Kaikōura, New Zealand, earthquake from optical image correlation: implications for strain localization and long-term evolution of the Pacific-Australian plate boundary. Geochem. Geophys. Geosyst. 20, 1609–1628. https://doi.org/10.1029/2018GC007951.